이학석사학위논문

Supported Lipid Bilayer as Biosensing Platform

바이오센싱 플랫폼으로서의 인지질이중층

2017년 8월

서울대학교 대학원

화학부 무기화학 전공

황 우 성

Supported Lipid Bilayer as Biosensing Platform

지도교수 남 좌 민

이 논문을 이학 석사학위논문으로 제출함

2017년 8월

서울대학교 대학원
화학부 무기화학 전공
황 우 성

황우성의 석사학위논문을 인준함

2017년 8월

위 원 장	이 동 환	(인)
부 위 원 장	남 좌 민	(인)
위 원	김 지 환	(인)

Supported Lipid Bilayer as Biosensing Platform

by Woosung Hwang

Thesis Advisor : Prof. Jwa-Min Nam

A Thesis for M.S. Degree in Inorganic Chemistry

Graduate School

Seoul National University

Abstract

Supported Lipid Bilayer as Biosensing Platform

Woosung Hwang

Department of Chemistry

The Graduate School

Seoul National University

It is difficult to continuously observe the behaviors of nanosized materials with existing equipment and experimental methods. Using supported lipid bilayers(SLB) can solve these problems. SLB is an artificial cell membrane that retains the important biological characteristics of cell membranes, such as fluidity and affinity with cell membrane components, and is easy to assemble into a desired form. In this thesis, new methods for observing the behavior of optically stable plasmonic metal nanoparticles using a two-dimensional SLB as a platform are presented and obtaining meaningful results. SLB platform has fluidity, and a number of metal nanoparticles can be bind to its surface. The movement of metal nanoparticles bound to the surface is observed in real time. Specific behavior of surface-modified metal nanoparticles can induced by external stimuli. The plasmonic metal nanoparticles have a property that the scattering intensity is amplified when they are located at a certain distance or less. Therefore, the phenomenon that

metal nanoparticles are bonded by external stimuli can be observed and tracked in real time. In this thesis, biomaterial detection methods using two dimensional support lipid bilayers and plasmonic metal nanoparticles will be presented. In addition, it has been shown that the nanoparticle behavior can be controlled by various surface modifications, and it is confirmed that the SLB is suitable as the platform of the biosensor.

Research has been conducted on how to detect viruses quickly and accurately for decades. Detection methods using nanoparticles have also been proposed and studied. Various properties of nanoparticles have been used for detection. Especially, the unique nature of metal nanoparticles due to localized surface plasmons enables the detection of viruses through a variety of methods. The ability to easily modify a variety of ligands and biochemical materials also served as an advantage as a biosensing material. In Chapter 1, we detected the virus by attaching the antibody-coated nanoparticles to the surface of the supported lipid bilayer. We confirmed that the degree of near-field interaction between nanoparticles differs according to the concentration of virus through dark-field microscopy. It is experimentally demonstrated that viruses of unknown samples can be detected through this.

The development of semiconductor-based computing devices has transformed modern society. Molecular computing has been proposed as a complementary technology, but its impact is still insignificant. Conventional methods rely heavily on DNA with good practicality and general applicability. Numerous nucleic acid-based calculations from logic gates to neural networks have been demonstrated. However, the practical application of DNA-based

devices beyond proof-of-concept has not been driven by many limitations. In Chapter 2, we demonstrated the possibility of a new type of information processing platform by combining the chemical nature of the functional groups introduced into the nanoparticles and the fluidity of the SLB. It was confirmed that the nanoparticles on the SLB were assembled and decomposed by the metal ion and the external environment.

Multiplexed real-time analysis on multiple interacting molecules and particles is needed to obtain information on binding patterns between multiple ligands and receptors, specificity of bond formations and interacting pairs in a complex medium, often found in chemical and biological systems, and difference in binding affinity and kinetics for different binding pairs in one solution. In particular, multiplexed profiling of microRNA (miRNA) in a reliable, quantitative manner is of great demand for the use of miRNA in cell biology, biosensing and clinical diagnostic applications, and accurate diagnosis of cancers with miRNA is not possible without detecting multiple miRNA sequences in a highly specific manner. In chapter 3, we report a multiplexed molecular detection strategy with optokinetically (OK) coded nanoprobes (NPs) that show high photostability, distinct optical signals and dynamic behaviors on a SLB (OK-NLB assay). Metal NPs with three distinct dark-field light scattering signals [red (R), green (G) and blue (B)] and three different target miRNA halfcomplements were tethered to two dimensionally fluid SLB with mobile (M) or immobile (I) state. In situ single-particle monitoring and normalized RGB analysis of the optokinetically combinatorial assemblies between three M-NPs and three I-NPs with dark-field microscopy

(DFM) allow for differentiating and quantifying 9 different miRNA targets in one sample. The OK-NP-based assay enables simultaneous detection of multiple miRNA targets in a highly quantitative, specific manner within 1 hour, and can be potentially used for diagnosis of different cancer types. We validated the OK-NLB assay with single-base mismatched experiments and HeLa cell-extracted total RNA samples by comparing the assay results to the quantitative reverse transcription polymerase chain reaction (qRT-PCR) result.

Keywords : Supported Lipid Bilayer(SLB), Nanoparticle, Biosensor, Virus Detection, Ligand Computing, miRNA Detection

Student number : 2014-22419

Contents

Chapter 1

Virus Detection using Nanoparticle-Tethered Supported Lipid Bilayer

1.1. Introduction

The virus is contagious and is thought to cause a variety of diseases. Virus mediated disease is becoming a more serious problem because viruses can be replicated using host cells and transmitted to individuals. Early detection and identification of viruses is required to prevent infection, and many researchers have developed rapid and sensitive virus detection methods. In fact, viruses are detected in a variety of ways, including by use of biochemical interaction[1-2] or using a unique geometric shape of the viral protein shell.[3,4]

The virus consists of nucleic acid and capsid protein. These components can act as targets of the detection system through specific types of biochemical interactions depending on the manner of use. Using antigen-antibody interaction is a typical method for selectively capturing capsid proteins. These interactions enable selective and sensitive detection of viral proteins. When detecting a nucleic acid, the viral nucleic acid can be detected using a complementary sequence, which is also a sensitive and selective method.[4]

Representative methods using the above principle are ELISA and PCR.[5,6] Since these methods are costly and complex procedures and require a great deal of time, the necessity of developing other methods has been highlighted. Because of the various physical and chemical advantages of nanoparticles, they have been studied as virus detection agents over a long period of time. Nanoparticles have different properties depending on their constituents as well

as their size. The metal nanoparticles show a distinctive feature of local surface plasmon resonance (LSPR), which is defined as the interaction of free electron clouds and electromagnetic fields of metal nanoparticles.[7] The LSPR of metal nanoparticles provides vivid colors under light and amplifies optical signals such as Raman scattering by Raman dyes present in these particles.[8] In addition, metal nanoparticles interact with visible light to provide a powerful scattering signal for biosensing.[4, 9, 10]

Gold and silver nanoparticles are typical metal nanoparticles. These nanoparticles can be used for virus detection because they can be easily attached biomolecules such as antibodies on their surface.[11] In addition, the size of the entire analysis platform is reduced because the basic elements are made in nano-size. In addition, the use of metal nanoparticles enables the production of cost effective and point-of-care detection platforms. In this thesis, we introduce a new virus detection method. This will be a new guideline for nanoparticle-based virus detection methods.

1.2. Experimental section

Preparation of small unilamellar vesicles (SUVs)

The SLBs were formed on the lower cover glass by SUV vesicle fusion. The lipid in chloroform solution was mixed to have 97.2 mol% dioleoylphosphatidylcholine (DOPC), 0.3 mol% biotinylated dioleoylphosphatidylethanolamine (DOPE), and 2.5 mol% 1k poly(ethylene glycol)-DOPE. The lipid mixture was evaporated with a rotary evaporator, and the lipid film was thoroughly dried under a stream of nitrogen. The dried mixture was resuspended in deionized (DI) water and followed by three repetitive freeze-thaw cycles. The total lipid concentration was 2 mg/mL. The solution was extruded 31 times through a polycarbonate membrane with 100 nm pores at 25 °C. The SUV solution was kept at 4 °C until use.

Synthesis of plasmonic nanoparticles

Spherical gold nanoparticles (50 nm) were purchased from BBI Solutions (Cardiff, UK) for nanoparticles scattering green light.

Preparation of Nano-probe

The mixture of antibody at a concentration of 4 μM were incubated with 50 pM plasmonic nanoparticles for 2 h at room temperature. The ratio of biotinylated strands to target capturing strands are 1.5% for MG-NP. The

solution was adjusted to 10 mM PB and 0.1% (w/v) sodium dodecyl sulfate. Three aliquots of 1 M NaCl, and 0.01% sodium dodecyl sulfate (SDS) solution were added with 1 h interval between each addition to achieve a final concentration of 0.15 M. The mixture was heated at 55 °C for 10 min after each salt addition. The mixture was incubated overnight at room temperature. The suspension was washed by centrifugation, the supernatant removal, and the particles redispersion in 10 mM PB solution for three times.

Reaction chamber preparation

SLBs were formed inside a glass flow chamber, consisting of a top and bottom glass and a thermoplastic spacer. The top slide glass was drilled to form inlet and outlet holes and passivated with 10 mg/mL bovine serum albumin solution to block SLB formation. The bottom cover glass was sonicated for 10 min in chloroform, acetone, and DI water, respectively. After sonication, the bottom glass was cleaned with 1 M NaOH for 1h and thoroughly washed with DI water. The top and the bottom glasses were assembled with a sandwiched thermoplastic spacer by heating at 120 °C on a digital hot plate. The SUV solution was prepared to have 1 mg/mL of SUV, 75 mM of NaCl, and 10 mM of phosphate buffer. The solution was introduced into the flow chamber for 40 min to form SLBs. The volume of the flow chamber was 9 μL. Streptavidin (10 nM) in 150 mM NaCl phosphate buffered saline (PBS, 10 mM phosphate buffer, pH 7.5) was injected to the flow cell to bind to the biotinylated lipid for 1 h. The flow cell was washed

with 150 mM NaCl PBS twice at each step. NPs (1 to 10 pM) were reacted for 10 min to have optimized density of ~2500 NPs/14400 μm for NPs. The buffer was exchanged to 225 mM NaCl PBS for assay conditions.

Real-time monitoring of combinatorial assembly between NP and NP-SLB assays

The movement and combinatorial assembly between NPs on SLBs were observed with DF microscope (Axiovert 200M, Carl Zeiss, Germany) with 40× objective lens (NA = 0.6) and AxiCam HR color camera. To characterize association of NP and to obtain a calibration curve, the antibody was supported by the BioNano Health-Guard Research Center. Known concentrations of targets virus in 150 mM NaCl PBS were injected into the reaction chamber. The NP binding events were monitored with DFM. Snapshot images were taken with 20 seconds interval for 30 minutes, and the assembly events in 120 × 120 μm area were counted. It should be noted that the calibration curves for detection targets of interest need to be calculated only one time, and the pre-obtained calibration curves can be used for actual assays. Three replicate samples were analyzed. The images were analyzed using ImageJ software (https://imagej.nih.gov/ij/).

1.3. Results and discussion

We observed the binding of antibody-bound nanoparticles on the SLB by viruses. Biotinylated DNA was attached to the nanoparticles used and ligated to the SLB surface using biotin-streptavidin interaction. A large number of nanoparticles were attached, and more than 70% of them were actively moving. The binding of nanoparticles was confirmed by looking at the near-field interaction phenomenon using dark-field microscopy. The nanoparticles connected to the SLB by biotin-streptavidin interaction move together as the lipid moves. That is, they diffuse freely on a two-dimensional plane (Figure 1.1b). When the distance between metal nanoparticles is less than their diameters, the near-field interaction phenomenon becomes prominent. The increase in the scattering intensity can be confirmed by dark-field microscopy. In the absence of a target virus that specifically binds to an antibody attached to the nanoparticle, the binding between the nanoparticles is not achieved. That is, the distance can be nearer as it diffuses freely, but it will soon be far away. The near-field interaction between these nanoparticles also exists only momentarily. In the presence of target virus, nanoparticles that are freely diffusing on the SLB surface can be bound via the virus. In this case, the nanoparticles maintain a close distance and the near-field interaction continues (Figure 1.1b). A calibration curve between the binding event and the virus concentration was obtained using various concentrations of virus samples (Figure 1.3). As the amount of target

virus increased, the number of bound nanoparticles increased at the same time. In the current system, detection was possible up to about 1000 $TCID_{50}$ /mL for Influenza A virus subtype H1N1. We also experimented with non-target viruses that do not specifically bind to antibodies attached to nanoparticles. The number of nanoparticles bound by a high concentration of non-target virus was lower than that of target virus 1000 $TCID_{50}$/mL. Taken together, our system using nanoparticles and SLB can selectively and specifically detect Influenza A virus subtype H1N1 up to 1000 $TCID_{50}$/mL through approximately 30 minutes of analysis. It would be similarly applicable to other antibody-virus or antibody-protein and would be available as a multiple detection system.

1.4. Conclusion

We have confirmed that a system combining antibody-modified nanoparticles with a SLB specifically detects the target virus. Several things need to be improved in order to be used for point-of-care detection. First, a lower detection limit and a shorter detection time must be met. In addition, detection of various types of viruses and proteins other than the H1N1 pandemic virus used in the thesis should be implemented by attaching different kinds of antibodies to the nanostructure. The final goal is to develop a system that can detect multiple types of biomolecules using various types of antibodies. SLB and nanoparticle-based methods are expected to be useful guidelines for the development of new nanoparticle-based methods for virus detection in the future.

1.5. References

1. J. R. Choi, J. Hu, S. S. Feng, W. A. W. Abas, B. Pingguan-Murphy, F. Xu, *Biosens. Bioelectron.* 2015, *79*, 98-107.

2. A. Kaushik, S. Tiwari, R. D. Jayant, A. Marty, M. Nair, *Biosens. Bioelectron.* 2016, *75*, 254-272.

3. A. Cumbo, B. Lorber, P. F.-X. Corvini, W. Meier, P. Shahgaldian, *Nat. Commun.* 2013, *4*, 1503-1507.

4. J.-E. Park, K. Kim, Y. Jung, J.-H. Kim, J.-M. Nam, *ChemNanoMat.* 2016, *2*, 927-936.

5. B. R. S. Yalow, S. A. Berson, *J. Clin. Invest.* 1960, *39*, 11-13.

6. R. K. Saiki, D. H. Gelfand, S. Stoffel, S. J. Scharf, R. Higuchi, G. T. Horn, K. B. Mullis, H. A. Erlich, *Science* 1988, *239*, 487-491.

7. E. Hutter, J. H. Fendler, *Adv. Mater.* 2004, *16*, 1685-1706.

8. B. Sepffllveda, P. C. Angelom8, L. M. Lechuga, L. M. Liz-Marzán, *Nano Today* 2009, *4*, 244-251.

9. Y. Yang, J. Nam, *Anal. Chem.* 2009, *81*, 2564-2568.

10. Y. K. Lee, S. Kim, J.-W. Oh, J.-M. Nam, *J. Am. Chem. Soc.* 2014, *136*, 4081-4088.

11. P. D. Howes, R. Chandrawati, M. M. Stevens, *Science* 2014, *346*, 1247390-1247390.

Chapter 2

Nanoparticle-Ligand Computing on Supported Lipid Bilayer

2.1. Introduction

The development of semiconductor-based computing devices has transformed modern society. Molecular computing has been proposed as a complementary technology, but its impact is still insignificant.[1,2] Conventional methods rely heavily on DNA with good practicality and general applicability. Numerous nucleic acid-based calculations from logic gates to neural networks have been demonstrated.[3] However, the practical application of DNA-based devices beyond proof-of-concept has been limited for the following reasons. DNA computing relies on the collision and exchange of oligonucleotide strands in solution. As the "circuit" becomes larger and more complex, the process becomes slower and less reliable. This inherent property greatly impairs the robustness of the signal output. Because computing algorithms are implemented directly with the nucleic acid itself, it is essentially impossible to distinguish between hardware and software. This ambiguity limits the module structure of the circuit because both the input, circuit, and output DNA strands are mixed in a single reaction vessel.[4] Moreover, changes in the physical properties of circuits due to computing results are inherently irreversible, resulting in limited usability. Most existing devices built on top of Bulk solution-based technology only output an ensemble average signal. The interactions between free diffusion molecules that make up a circuit can not be tracked or quantified individually.[2]

We will develop a programmable two-dimensional (2D) nano tablet as a

fluid platform that can inspire and be able to simultaneously track and track multiple chemical events with superior efficiency, accuracy and versatility inspired by the cell membrane.[5] As with electronic devices, programmable nano-tablets consist of hardware and software components. Hardware includes lipid membranes, nanoparticles (NP), and ligands. Software is a set of instruction and logic circuits that are operated by a dynamic network of lipid-NP-ligand interactions (Figure 2).

Following a series of logic, we will implement and improve the following key design principles by changing the dynamic assembly and disassembly of nanoparticles into a collective network. Conventional NP systems operate on bulk (3D) solutions. Conversely, our nano-tablets utilize a lipid bilayer as a fluid platform to confine NP motion to 2D space, while at the same time facilitating diffusion for dynamic assembly and disassembly of the ligand-bound NP.[5,6] These membrane-based 2D reaction spaces enable (i) high-resolution in-situ imaging of NP and chemical processes and (ii) iterative, efficient write-read-erase cycles.[7] The Nano Tablet platform needs to dramatically expand the range of 'computable molecules' beyond the traditional Watson-Crick base pairs.

The input signal is processed not by structural or functional complementarity between two interacting molecular species but by group interaction between NPs through various chemical interactions (eg, hydrogen-bonding donor-acceptors, metal ligands).[8] Combined with microfluidics and ultrasensitive wide-field imaging techniques, the throughput of programmable nano-tablets will be greatly improved. The inherent

reversibility of the NP-NP assembly / disassembly process makes the logic operation reversible and adjustable. A write-read-erase cycle should be the ideal test bed for implementing and improving these concepts. Calculation with nano-tablets takes advantage of diffusion-collision interactions confined to the 2D fluid space. The reaction rate (= data processing rate) can be easily controlled by changing the fluidity of the lipid bilayer or the valence control of NP. By processing the signal through statistical analysis from single particle to population level, you can reduce the probabilistic noise of each circuit. The above functions enable a sensitive and reliable evaluation of NP assembly events.

2.2. Experimental Section

Preparation of small unilamellar vesicles (SUVs)

The SLBs were formed on the lower cover glass by SUV vesicle fusion. The lipid in chloroform solution was mixed to have 97.2 mol% dioleoylphosphatidylcholine (DOPC), 0.3 mol% biotinylated dioleoylphosphatidylethanolamine (DOPE), and 2.5 mol% 1k poly(ethylene glycol)-DOPE. The lipid mixture was evaporated with a rotary evaporator, and the lipid film was thoroughly dried under a stream of nitrogen. The dried mixture was resuspended in deionized (DI) water and followed by three repetitive freeze-thaw cycles. The total lipid concentration was 2 mg/mL. The solution was extruded 31 times through a polycarbonate membrane with 100 nm pores at 25 °C. The SUV solution was kept at 4 °C until use.

Synthesis of plasmonic nanoparticles

Spherical gold nanoparticles (50 nm) were purchased from BBI Solutions (Cardiff, UK) for nanoparticles scattering green light.

Preparation of Nano-Probe

The mixture of thiolated strands at a concentration of 4 μM were incubated with 50 pM plasmonic nanoparticles for 2 h at room temperature. The ratio of biotinylated strands to target capturing strands are 1.5% for

MG-NP. The solution was adjusted to 10 mM PB and 0.1% (w/v) sodium dodecyl sulfate. Three aliquots of 1 M NaCl, and 0.01% sodium dodecyl sulfate (SDS) solution were added with 1 h interval between each addition to achieve a final concentration of 0.1 M. The mixture was heated at 55 °C for 10 min after each salt addition. The mixture was incubated overnight at room temperature. The suspension was washed by centrifugation, the supernatant removal, and the particles redispersion in 10 mM PB solution for three times.

Reaction chamber preparation

SLBs were formed inside a glass flow chamber, consisting of a top and bottom glass and a thermoplastic spacer. The top slide glass was drilled to form inlet and outlet holes and passivated with 10 mg/mL bovine serum albumin solution to block SLB formation. The bottom cover glass was sonicated for 10 min in chloroform, acetone, and DI water, respectively. After sonication, the bottom glass was cleaned with 1 M NaOH for 1h and thoroughly washed with DI water. The top and the bottom glasses were assembled with a sandwiched thermoplastic spacer by heating at 120 °C on a digital hot plate. The SUV solution was prepared to have 1 mg/mL of SUV, 75 mM of NaCl, and 10 mM of phosphate buffer. The solution was introduced into the flow chamber for 40 min to form SLBs. The volume of the flow chamber was 9 μL. Streptavidin (10 nM) in 150 mM NaCl phosphate buffered saline (PBS, 10 mM phosphate buffer, pH 7.5) was injected to the flow cell to bind to the biotinylated lipid for 1 h. The flow cell was washed

with 150 mM NaCl PBS twice at each step. NPs (1 to 10 pM) were reacted for 10 min to have optimized density of ~2000 NPs/14400 μm for MG-NP . The buffer was exchanged to 75 mM NaCl PBS for assay conditions.

Real-time monitoring of combinatorial assembly between NP and NP-SLB assays

The movement and combinatorial assembly between OK-NPs on SLBs were observed with DF microscope (Axiovert 200M, Carl Zeiss, Germany) with 40× objective lens (NA = 0.6) and AxiCam HR color camera. To characterize association of NP and to obtain a calibration curve, the iron(III) nitrate was purchased from Sigma-Aldrich. Known concentrations of iron(III) nitrate in 75 mM NaCl PBS were injected into the reaction chamber. The negative control sample contains 500 nM of copper(II) nitrate. The NP binding events were monitored with DFM. Snapshot images were taken with 10 min interval for 1 h, and the assembly events in 120 × 120 μm^2 area were counted. It should be noted that the calibration curves for detection targets of interest need to be calculated only one time, and the pre-obtained calibration curves can be used for actual assays. Three replicate samples were analyzed. The images were analyzed using ImageJ software (https://imagej.nih.gov/ij/).

2.3. Results and Discussion

Catechol is a frequently seen ligand in bioactive materials such as enterobactin, and exhibits a very strong binding affinity with pH & redox-responsive and Fe^{3+}. Therefore, catechol ligands are suitable for controlling AuNP assembly using external stimuli such as pH, redox reagent and Fe^{3+}. In order to modify these catechol structures into nanoparticles, ligands were designed as shown in Fig. 2.1. The thiol group was introduced for the modification of the plasmonic nanoparticles, and AuNP assembly experiments were carried out in aqueous condition, so thiol and catechol were connected using a water-soluble tetraethyleneglycol linker.

First, we observed the Fe^{3+}-induced assembly in solution to confirm that the ligand introduced into the nanoparticles was working properly. The surface of gold nanoparticles was modified by varying the ratio of 1k thiol-mPEG to ligand, and whether catechol ligands specifically bound Fe^{3+} in solution was analyzed by UV-Vis analysis(Figure 2.2). When gold nanoparticles were modified with the ratio of ligand to PEG of 1: 1 and Fe^{3+} was added, a new peak appeared at a wavelength of 560 nm where the absorbance peak decreased to about 650 nm. In addition, when the ligand and PEG were introduced into the gold nanoparticles at a ratio of 1:40, the peak around 560 nm became wider and redshift when Fe^{3+} was added. The UV spectra of gold nanoparticles, gold nanoparticles + Fe^{3+}, and Fe^{3+} were measured to see if there was a change in the UV spectrum due to

nonspecific reaction between nanoparticles and Fe^{3+}. As a result, Fe^{3+} did not exhibit any UV absorbance, and the peaks of gold nanoparticles and AuNP + Fe^{3+} were almost identical, suggesting that non-specific binding between nanoparticles and Fe^{3+} did not occur. In general, when the nanoparticles aggregate or increase in size, the intensity of the original AuNP peak (around 560 nm) is partially reduced and a new peak appears in the red-shifted region. In other words, this change in the peak of the UV spectrum is indirect evidence to demonstrate the formation of dimers or even multimers by specific chelation between the ligand and Fe^{3+}.

Next, we observed the Fe^{3+}-induced assembly of the nanoparticles modified with ligands on SLB. The nanoparticles used above were attached to the SLB using biotin-streptavidin interaction(Figure 2.3). A large number of nanoparticles were attached, and more than 70% of them were actively moved to prepare an environment for observing the Fe^{3+}-induced assembly. Fe^{3+} was added to the SLB system and observed for 30 minutes in real time(Figure 2.4). Looking at the red circle in the figure 2.4, we can see that the scattering intensity is increased. This means that the nanoparticles are constrained to a very short distance, and the binding of the nanoparticles is achieved through the combination of chemical ligands and ions.

We confirmed that the model system using catechol was Fe^{3+}-induced assembly on the solution phase and SLB, and made it faster and quantitatively by probe optimization. When using conventional gold nanoparticles, high nanoparticle density could be obtained on SLB, resulting in a greater number of binding events. However, too high a nanoparticle density

will cause problems later in the experimental step and rewritable. In order to solve this problem, the probe was optimized so that the number of nanoparticle densities was reduced and more than a certain number of binding events occurred. The binding between the nanoparticles via the Fe^{3+}-induced assembly was clearly distinguished by comparison with the control group through observation for 30 minutes(Table 2.1 and Figure 2.5a).

The Fe^{3+}-induced assembly on the SLB was disassembled by three methods: pH change, EDTA addition, and excess free catechol addition. In order to disassembly the assembled probe, it is necessary to reduce the binding force between catechol and Fe^{3+} or eliminate Fe^{3+}, which can bind to catechol. The pH change changes the chemical properties of catechol and reduces the binding force with Fe^{3+}. EDTA and excess free catechol have the effect of removing Fe^{3+} by binding to Fe^{3+} used in the assembly. Among the three methods, the free chatechol method was most effective.

2.4. Conclusion

A new chemical, biological platform that can directly convert molecular phenomena into easily observable signals will have a significant impact on both science and technology. We aim to achieve this goal by developing a programmable nano-tablet, a nanoparticle based write-read-erase device that processes molecular information through massively parallel logic operations. There is originality in that it suggests and utilizes a new paradigm by making use of methods that have not been attempted until now, called logical operators that utilize nanoparticles, molecular recognition, cell membrane fluidity. As a technical application of this new device platform, our initial efforts focused on the assembly and disintegration of ligand-attached nanoparticles by the external environment on the SLB.

We have synthesized a pH & redox-responsive model ligand with a thiol group that can be attached on the AuNP, and a synthetic pathway that can control the length and ligand type of the linker in various ways. We have confirmed that the gold nanoparticles modified with chemical ligands on the solution phase and membrane membrane nano tablets are assembled by Fe^{3+}. The three external stimuli (EDTA, pH, catechol) showed degradation of the assembled-nanoparticles, indicating the possibility of an on/off system. In addition to catechol-based ligands, we have also developed a relatively soft terpy-based ligand. In order to develop a new type of information processing platform by combining the chemical properties of various molecules and functional groups introduced into the nanostructures and the fluidity of the

lipid bilayers, the following contents will be achieved first.

We will study how the basic kinetics and thermodynamics of ligands introduced on nanoparticle surfaces bind to metals to form nanoparticle assemblies differ from bulk solutions. Particularly, on the surface of nanoparticles, PEG chains are introduced in addition to synthesized ligands. It is possible to control the steric around the ligand by controlling the relative length between the PEG chains at the periphery of the ligand and the synthesized ligand. This type of steric control is not possible in bulk solutions. The advantage of the cell membrane nano-tablet is that it can check the progress of the program in real time and can be used repeatedly. For the Fe^{3+} induced assembly system to meet this requirement, most of the assembled nanoparticles must be disassembled under disassembly conditions. The pH change, EDTA addition, and free catechol addition method had many undissociated nanoparticles. We will improve it and implement repeatable and rewritable properties. A "synthetic pathway" for easy synthesis of various ligands was developed as shown in Fig 2.6a. Using the synthetic pathway developed during the synthesis of the model ligand, a molecule with a terminal alkyne instead of catechol can be made as shown in Fig 2.6a. This method is convenient because it allows introduction of various ligands at the end of the synthesis with click chemistry. Through the above synthesis pathway, we will synthesize ligands capable of assembling and disassembling nanoparticles by a mechanism different from that of catechol. It will be shown that the assembly and disassembly of nanoparticles incorporating these ligands on SLB can be controlled using pH, light, redox reagent, and the like.

This method of operation can provide faster and more accurate results than a specific material-based assembly such as a target. Nanoparticles with different ligands are reacting differently depending on how they work, so they can perform multiple signals and functions. We will make sure that each ligand works independently without interference, and implement logic gates such as AND, OR logic gates on SLB based on this.

2.5. References

1. Seelig, G., Soloveichik, D., Zhang, D. Y., Winfree, E., *Science* 2006, *314*, 1585-1588.

2. Qian, L., Winfree, E., Bruck, J., *Nature* 2011, *475*, 368-372.

3. Prokup, A., Hemphill, J., Deiters, A. *J. Am. Chem. Soc.* 2012, *134*, 3810-3815.

4. Jung, C., Ellington, A. D., *Acc. Chem. Res.* 2014, *47*, 1825-1835.

5. Lee, Y. K., Kim, S., Oh, J.-W., Nam, J.-M., *J. Am. Chem. Soc.* 2014, *136*, 4081-4088.

6. Yashin R., Rudchenko, S., Stojanovic, M. N., *J. Am. Chem. Soc.* 2007, *129*, 15581-15584.

7. Ota, S., Wang, S., Wang, Y., Yin, X., Zhang, X., *Nano Lett.* 2013, *13*, 2766-2770.

8. Huschka, R., Zuloaga, J., Knight, M. W., Brown, L. V., Nordlander, P., Halas, N. J., *J. Am. Chem. Soc.* 2011, *133*, 12247-12255.

Chapter 3

Optokinetically Encoded Nanoprobe-Based Multiplexing Strategy for MicroRNA Profiling

3.1. Introduction

It is important to obtain dynamic interaction between nanoparticles or molecules in real time with accurate and high resolution. In particular, if a large number of interactions can be obtained by individual particles, various chemical and biological principles can be found and applied to various applications.[1,2] The ability to obtain images with a single nanoparticle-level resolution in real-time allows us to see how the individual nanoparticles behave in dynamic motion, and thus we can reliably differentiate the unique interactions of specific nanoparticles among many of the nanoparticles.[3] This can provide direct and specific information on the assembly mechanism of nanoparticles and the kinetics of molecular-level reactions.[3] However, currently available high-resolution image methods such as electron microscopes provide only static information for a limited number of types.[4] Moreover, they can not provide real-time information and require complex experimental procedures and harsh conditions.[3] In order to observe the interaction of the individual nanoparticles in real time, the methods such as liquid transmission electron microscopy have been developed, but they can only be used in limited situations due to the particle-affecting characteristics at the observation stage. To overcome this problem, fluorescence-based methods were used for individual-nanoparticle-level imaging, but there were problems such as photo-bleaching and photo-blinking of the chromophore.[5] Moreover, the characteristics of fluorescence molecules, including fluorescence

transfer energy transfer, are difficult to observe the interaction of multiple particles. Another important issue is whether a single nanoparticle-level imaging can be sustained over a long period of time.[5] In a typical experimental environment, the nanoparticles are freely diffusing in three dimensions, so the microscope focuses on and out repeatedly. This makes it difficult to observe and track numerous nanoparticles at the same time. Therefore, methods for overcoming these problems have been continuously demanded, and the method of imaging and analyzing freely moving nanoparticles at real time with individual particle level is very valuable.[6] In order to obtain useful statistical information and derive a new principle from it, several interactions must be analyzed at the resolution of the individual particle level at the same time.

In order to make this possible, we introduced surface-modified plasmonic nanostructures into the surface of a two dimensional fluidic supported lipid bilayer with controlled their mobility. Two-dimensional moving nanostructures on liquid SLBs can be traced individually by dark-field microscopy. As the repetitive focus in and focus out, which occurs when moving freely in a 3D environment, is limited to a two-dimensional environment, effective and continuous observation becomes possible. DNA-modified nanoparticles can be bound to each other through DNA hybridization, and plasmonic coupling caused by bond formation can be observed in dark-field microscopy in real time and provides kinetic information.

Multiparallel reactions among a variety of reactants are common phenomena in chemical and biological systems.[7-9] Simultaneous interpretation

of multiple interactions from complex reaction mixtures offers important chemical or biological information including binding affinity and nature, reaction mechanisms, reaction and binding specificity, biodiagnostics, and rapid screening in biological sensing.[10] It is, however, challenging to distinguish multiple interactions in a single reaction mixture due to the lack of tools for obtaining reliable information on complex binding events and their kinetic information with multiple (or multiplexed) readouts.[11]

MicroRNAs (miRNAs) are small (~22-nt), single stranded, noncoding RNAs. miRNAs act as post-transcriptional gene regulators and have emerged as potential diagnostic and prognostic biomarkers for human diseases including cancers and neurodegenerative diseases.[12-14] The capability to identify and quantify multiple miRNA species is critical in translating miRNA sequences into useful information and is highly beneficial for improving the accuracy, precision, and specificity of diagnosis.[15] Accurate quantification of miRNA is, however, difficult due to its intrinsically short length and instability.[16] Although the quantitative reverse transcription polymerase chain reaction (qRT-PCR) offers high sensitivity and specificity, it requires poly-A tail or specially designed primer in cDNA formation and error-prone enzymatic amplification and is relatively low-throughput.[17] Microarrays are high-throughput, but they use fluorescence-based quantification that provides only relative expression values.[17] Recently, researchers have developed nanostructure-based miRNA detection methods that use biobarcode amplification,[18] nanopores,[19] gold nanoparticles,[20] scanometric arrays,[21] silicon nanowires,[22] graphene oxide,[23] and quantum dots.[24] However, previously

reported nanostructure-based assays have limited multiplexing and quantification capabilities, and the assay time is typically well over 1 h with complicated multiple reaction steps and setups. Further, fluorescence-based methods including PCR and microarrays have limitations in photostability and multiplexing capability of fluorophore probes. Therefore, it remains challenging to develop a miRNA identification and quantification method that meets both speed and multiplexed detection requirements.

Here, we developed an optokinetically encoded plasmonic nanoprobe-based multiplexing strategy, and this strategy was used for miRNA profiling to identify and quantify 9 different miRNA species simultaneously on two-dimensional (2D) supported lipid bilayer (SLB) (Figure 3.1). The nanoprobes (NPs) here are coded optically (combinatorial plasmonic couplings) and kinetically (particle mobility) to generate highly multiplexed detection of targets (Figure 3.1). In DNA design, first, three different oligonucleotide sequences for detecting three different miRNA sequences and biotinylated DNA for tethering NPs to biotinylated SLB via streptavidins were modified to each NP. The number of modified biotinylated DNA strands per particle determines the mobility of probes for the kinetic coding (low biotin valency, mobile (M) probes; high biotin valency, immobile (I) probes).[25] For the optical coding, three different plasmonic nanostructures with distinctively different light scattering spectra [red (R), green (G), and blue (B) color-scattering nanostructures] were used (Figure 3.1 and Figure 3.2b). Six types of optokinetically encoded NPs (MR-, MG-, MB-, IR-, IG-, and IB-NPs) were identified at single-particle level by real-time monitoring of

their distinct scattering signals using dark-field microscopy (DFM). DNA sequences were

modified to NP in a way that mobile NPs interact only with immobile NPs while M-NPs (or I-NPs) do not interact with other M-NPs (or I-NPs). It should be noted that target capturing induces assemblies of NPs and plasmonic coupling between NPs. The plasmonic coupling between different nanostructures generates unique scattering signal change, which is detectable and identifiable by DFM in a highly parallel manner (Figures 3.2a,c). Colorimetric signal change due to plasmonic coupling at the single nanoparticle-level was quantitatively analyzed with RGB color profiling method.

With this optokinetic (OK) coding strategy and highly photostable DFM-based single-particle analysis method on distinct plasmonic coupling, 9 different interactions between NPs induced by 9 different targets can be clearly distinguishable and detected on 2D SLB. Based on these designs and principles, we developed the OK-NP-tethered SLB (OKNLB) assay. These nine NP assembly reactions were quantitatively analyzed as analogues of multicomponent association reactions (Figure 3.2b). Target miRNA sequences were selected based on the previous reports showing their abnormal expression patterns in multiple cancers.[26-28] In principle, one can potentially differentiate and diagnose prostate, breast, and lung cancers by identifying these 9 miRNA targets in one sample. The OK-NLB assay was further validated with HeLa cell-extracted total RNA samples for 9 different RNA sequences, and the results were compared to the qRT-PCR.

3.2. Experimental Section

Preparation of small unilamellar vesicles (SUVs)

The SLBs were formed on the lower cover glass by SUV vesicle fusion. The lipid in chloroform solution was mixed to have 97.2 mol% dioleoylphosphatidylcholine (DOPC), 0.3 mol% biotinylated dioleoylphosphatidylethanolamine (DOPE), and 2.5 mol% 1k poly(ethylene glycol)−DOPE. The lipid mixture was evaporated with a rotary evaporator, and the lipid film was thoroughly dried under a stream of nitrogen. The dried mixture was resuspended in deionized (DI) water and followed by three repetitive freeze-thaw cycles. The total lipid concentration was 2 mg/mL. The solution was extruded 31 times through a polycarbonate membrane with 100 nm pores at 25 °C. The SUV solution was kept at 4 °C until use.

Synthesis of plasmonic nanoparticles

Gold nanorods with an aspect ratio value of 4 were synthesized for red NPs by a seed-mediated growth mechanism. The seed was prepared by mixing 5 mL of 0.5 mM $HAuCl_4 \cdot 3H2O$ solution with 5 mL of 0.2 M cetyl trimethylammonium bromide (CTAB), followed by rapid injection of 600 μL of ice-cooled 0.01 M NaBH4 solution. The seed solution was kept for 2 h after reducing step. A 5 mL aliquot of 0.5 mM $HAuCl_4 \cdot 3H2O$ solution was mixed with 5 mL of 0.2 M CTAB solution, and 250 μL of 4 mM AgNO3 solution was added, followed by 70μL of 78 mM ascorbic acid solution. Seed solution

(12 μL) was added and gently mixed. The solution was incubated for 4 h. To enhance scattering intensity, we coated the gold nanorods with thin silver shells. Gold nanorods (1 mL, 100nM) were mixed with cetyl trimethylammonium chloride (1 mL, 10 mM), $AgNO_3$ (1 mL, 0.2 mM), and ascorbic acid (1mL, 50 mM). After 4 h incubation, the solution was washed for three times by centrifugation, supernatant removal, and redispersion in DI water. Spherical gold nanoparticles (50 nm) were purchased from BBI Solutions (Cardiff, UK) for nanoparticles scattering green light. To synthesize nanoparticles scattering blue light, we formed 20 nm silver shells on 20 nm gold seed. Two hundred microliters of mixture was prepared to obtain 150 pM of 20 nm gold nanoparticle (BBI Solutions, Cardiff, UK), 0.2% polyvinylpyrrolidone (PVP), and 0.25 mM $AgNO_3$. Sodium ascorbate solution (100 μL, 50 mM) was rapidly injected into the mixture to form a silver shell and the color turned yellow immediately. This solution was directly used for DNA modification for particle stability. The TEM images are obtained using JEM-2100 (JEOL) systems at the National Center for Inter-University Research Facilities (NCIRF), Korea.

Preparation of OK-NPs

Synthetic thiolated oligonucleotides (Bioneer, Daejeon, Korea) were reduced by incubation with 100 mM dithiothreitol (DTT) in 100 mM phosphate buffer (PB) solution for 1 h and separated with an NAP-5 column (GE Healthcare, Buckinghamshire, U.K.). For detailed sequences of thiolated

oligonucleotides attached on each OK-NP, see Table 3.3. The mixture of thiolated strands at a concentration of 4 μM were incubated with 50 pM plasmonic nanoparticles for 2 h at room temperature. The ratio of biotinylated strands to target capturing strands are 1%, 0.1%, 0.5%, and 30% for MR-NP, MG-NP, MB-NP, and I-NP, respectively. The solution was adjusted to 10 mM PB and 0.1% (w/v) sodium dodecyl sulfate. Three aliquots of 1 M NaCl, and 0.01% sodium dodecyl sulfate (SDS) solution were added with 1 h interval between each addition to achieve a final concentration of 0.3 M. The mixture was heated at 55 °C for 10 min after each salt addition. The mixture was incubated overnight at room temperature. The suspension was washed by centrifugation, the supernatant removal, and the particles redispersion in 10 mM PB solution for three times.

Reaction chamber preparation

SLBs were formed inside a glass flow chamber, consisting of a top and bottom glass and a thermoplastic spacer. The top slide glass was drilled to form inlet and outlet holes and passivated with 10 mg/mL bovine serum albumin solution to block SLB formation. The bottom cover glass was sonicated for 10 min in chloroform, acetone, and DI water, respectively. After sonication, the bottom glass was cleaned with 1 M NaOH for 1h and thoroughly washed with DI water. The top and the bottom glasses were assembled with a sandwiched thermoplastic spacer by heating at 120 °C on a digital hot plate. The SUV solution was prepared to have 1 mg/mL of SUV, 75 mM of NaCl, and 10 mM of phosphate buffer. The solution was

introduced into the flow chamber for 40 min to form SLBs. The volume of the flow chamber was 9 μL. Streptavidin (10 nM) in 150 mM NaCl phosphate buffered saline (PBS, 10 mM phosphate buffer, pH 7.5) was injected to the flow cell to bind to the biotinylated lipid for 1 h. The flow cell was washed with 150 mM NaCl PBS twice at each step. NPs (1 to 10 pM) were reacted for 10 min to have optimized density of ~700 NPs/14400 μm^2 for each M-NP and ~1200 NPs/14400 μm^2 for each I-NP. The buffer was exchanged to 225 mM NaCl PBS for assay conditions.

Cell Culture

HeLa (human epithelial carcinoma line; ATCC, Num. CCL-2) cells were purchased from the Korean Cell Line Bank (Seoul, Korea). The cells were cultured in RPMI medium (Gibco, USA) containing 10% fetal bovine serum, 100 U/mL penicillin, and 100 μg/mL streptomycin (Gibco, USA). The cell line was incubated at 37 °C with 5% CO2 in a humidified incubator.

Total RNA extraction from HeLa cells

We used the Qiagen miRNeasy miRNA extraction kit (Hilden, Germany) which isolates total RNA (>18 nucleotides) through phenol/guanidine-based lysis of samples and silica membranebased purification. Eighty percent of confluent cells grown in a monolayer in 75 cm^2 flask were trypsinized and transferred to a clean 2 mL microcentrifuge tube. After centrifugation at 300 × g for 5 min the cells were collected as a cell pellet and the supernatant

was completely aspirated. The cell pellet was mixed with 700 μL QIAzol Lysis Reagent, homogenized by vortexing, incubated for 5 min at room temperature, and subsequently mixed with 140 μL chloroform. The organic and aqueous phase was separated by centrifugation for 15 min at 12,000 × g at 4 °C. The aqueous phase containing the RNA was carefully transferred to a new collection tube and mixed with 1.5 volumes of 100% ethanol. The mixture was loaded into an RNeasy Mini spin column and washed several times at 8100 × g. The RNeasy Mini column was transferred to a clean 1.5 mL collection tube, and RNA was eluted by addition of 50 μL RNase-free water. The total RNA concentration was 120 ng/μL with A_{260}/A_{280} = ~2. The cell extract was kept frozen until use.

Real-time monitoring of combinatorial assembly between OK-NPs and OK-NLB assays

The movement and combinatorial assembly between OK-NPs on SLBs were observed with DF microscope (Axiovert 200M, Carl Zeiss, Germany) with 40× objective lens (NA = 0.6) and AxiCam HR color camera. To characterize association of OK-NPs and to obtain a calibration curve, the synthetic miRNAs were purchased from Bioneer (Daejeon, Korea) (Table 3.3). Known concentrations of miRNA targets in 225 mM NaCl PBS were injected into the reaction chamber. The negative control sample contains 300 pM of miR-100. The NP binding events were monitored with DFM. Snapshot images were taken with 10 min interval for 1 h, and the assembly events in

120 × 120 μm^2 area were counted. It should be noted that the calibration curves for detection targets of interest need to be calculated only one time, and the pre-obtained calibration curves can be used for actual assays. For the HeLa cell assay, cell extracts were diluted to a final concentration of 600 ng/μL in 225 mM NaCl PBS and injected into the reaction cell. Three replicate samples were analyzed. The images were analyzed using ImageJ software (https://imagej.nih.gov/ij/).

qRT-PCR analysis

The qRT-PCR analysis of cell extracts was performed using Geno-Total RNA Kit (Genolution, Seoul, Korea). cDNA was synthesized from total RNA sample with the Mir-X kit (Clontech). A SYBR Green-based qRT-PCR reaction was conducted with the real-time PCR system (Bio-Rad CFX) using Geno-qPCR kit no. RD1101 (Genolution, Seoul, Korea). PCR was carried out with initial denaturation at 95 °C for 2 min, followed by 40 cycles of 95 °C for 5 s and 60 °C for 20 s. Relative expressions of each miRNA to U6 snRNA as an internal control were calculated by the $2^{-\triangle CT}$ method. The reactions were run in duplicate to obtain standard deviations.

3.3. Results and Discussion

In a typical experiment, we prepared DNA-modified nanoparticles and tethered these particles to SLB. Three target capture DNA sequences that are half-complementary to target miRNA, were modified onto each OK-NPs **(Figure 3.1, Figure 3.2 and Table 3.3)**. For distinct optical encoding, we prepared three types of plasmonic nanoparticles that scatter red, green, and blue light by varying size, shape and composition to yield desirable optical properties. Gold nanorods with a silver shell (~46 nm in longer axis and ~ 13 nm in shorter axis with ~5 nm shell), gold nanospheres (~47 nm in diameter), and silver nanospheres on gold seeds (~19 nm core and ~37 in diameter) were synthesized and used as R-NPs, G-NPs, and B-NPs, respectively. The DFM images showed red, green, and blue scattering signals from the nanoparticles,

and R-NPs, G-NPs, and B-NPs showed the distinct localized surface plasmon resonance at different wavelengths in the extinction spectra (Figures 3.3a, b). Because of their distinct optical properties, we can individually identify R-, G-, and B-NPs from a mixture of densely tethered NPs on SLB (Figure 3.3c). The NPs were kinetically encoded on SLB by controlling the ratio of biotinylated (tethering group to streptavidin) DNA to target-capturing DNA on the nanoparticle surface. Biotinylated DNA can be bound to biotinylated SLB via multivalent streptavidin linkers. The particles with a low valency were tethered with high mobility, whereas the particles with a high valency were immobilized by forming multiple linkages between the particles and the

SLB.[14] M-NPs showed random 2D Brownian motion confirmed by linear mean square displacement plot (Figures 3.4a,b). Nearly 90% of M-NPs were mobile on SLB (Figure 3.4c). The lipid-tethered NPs occasionally exhibited a confined behavior and hop diffusion when observed for a prolonged period (>10 min), mainly because of incomplete homogeneity in lipid substrates.[29] Particle diffusion in fluid is explained by the Stokes-Einstein equation, which describes that hydrodynamic radius is inversely proportional to diffusion coefficients in 3D Brownian motion. Interestingly, the average diffusion coefficients of MR-, MG-, and MB-NPs were 0.362 ± 227, 0.383 ± 203, and 0.379 ± 202 $\mu m^2/s$, respectively. These results indicate that the diffusion of these mobile probes did not depend on the different hydrodynamic size of the NPs, which implies that the diffusion of the tethered NPs is mainly driven by the lateral mobility of lipids, and the kinetic encoding of NPs is decoupled with optical encoding. We also checked the photostability of OK-NPs on SLB under continuous illumination of dark-field light source for one hour (Figure 3.5a). Significantly, the RGB profiles of scattering intensities of red, green and blue probes were well maintained without photoblinking nor photobleaching for the whole observation period (60 min), indicative of high photostability of the light-scattering OKNPs on SLB. Next, we verified that the real-time monitoring of the six OK-NPs can differentiate 9 different types of plasmonic coupling signals based on different target miRNA-induced binding events (Figure 3.6). Without target addition, only transient scattering color changing events were observed due to temporary nonspecific overlaps between M-NPs and I-NPs. In the presence of the targets, the miRNAs were

hybridized with half complementary DNA strands on both M- and I-NPs, confining M-NPs to I-NPs to induce plasmonic coupling between particles. We interpreted and classified the types of association events using light-scattering signal changes in DFM images and RGB intensity profiles of each particle. R-, G-, and B-NP monomers were represented as distinct red, green, and blue spots in the DF image with the strongest red, green, and blue channel intensities, respectively, in RGB profiles (Figure 3.5b). Binding of MR-, MG-, and MB-NPs to an I-NPs increased red, green, and blue color intensities, respectively. Accordingly, the red, green and blue colors of R-R, G-G, and B-B homodimers are significantly brighter than R-, G-, and B-NP monomers. The R-G, G-B, and B-R heterodimers displayed orange, cyan, and magenta colors. The binding of a MR-NP to an I-NP only increased red color intensity with negligible changes in green and blue color intensities. Assembly with MG-NPs enhanced both red and green color intensities, whereas assembly with MB-NPs resulted in distinct change in blue color intensity. A red-shift of color profile in association among G- and B-NPs was observed as a result of a plasmonic coupling effect.[30] The formations of MG-IG dimer and MB-IB dimer induced higher R to G and G to B ratios, respectively, compared to their monomer states. The above in situ monitoring and color profiling strategy also can identify trimer formation (the addition of a third NP to dimer). However, in the case of tetramer formation (addition of the fourth NP to trimer, which is rare), it was challenging to differentiate which M-NP was engaged with the trimer, due to the complex plasmonic coupling arising from different geometric configurations. Therefore, we

controlled the density of I-NPs to be higher than that of MNPs to reduce multimer formation and thereby simplify data analysis. Due to heterogeneity in the size and optical signals of NPs, particle tracking should be initiated prior to the target addition to fully differentiate each NP assembly event with high reliability. All 9 types of different interactions were successfully discriminated and counted in a parallel manner over a large area (Figure 3.7).

Before obtaining a calibration curve, we analyzed the NP reaction kinetics. The binding events can be regarded as multi-component association reactions (Figure 3.2b and Equation 3.1).

$$\text{I-NP} + \text{M-NP} + \text{miRNA} \rightarrow \text{I-M complex} \qquad (1)$$

We first tested the effect of NP density on NP association reaction. Although we aimed to load a similar number of NPs on SLBs in different reaction chambers by controlling loading time and particle concentration, there were deviations in the NP density for each batch. The higher density of M-NPs and I-NPs resulted in an increased number of binding events for the same target concentration (Figure 3.8a and Table 3.1). When the number of binding events after 60 min incubation was proportional to $[\text{I-NP}]^{0.5}[\text{M-NP}]^{0.5}$, the lowest standard deviation and largest R^2 value were obtained (Figure 3.8b).

The logarithm of target concentration showed a linear behavior with the normalized binding events (Figure 3.10). By considering the NP density and target concentration factors, we can build the reaction kinetics equation for the OK-NP reaction.

$$\text{binding events} = k_{XY}\frac{[IX-NP]^{0.5}[MY-NP]^{0.5}}{1000\text{NPs/unit area}}$$

log([miRNA]/pM) (X, Y = R, G, B) (2)

where k_{XY} is reaction rate constant (1 hr), which represents the binding efficiency, [MX-NP] and [MY-NP] is the 2D NP density. To remove the effect of different NP density per reaction chamber, we used the normalized the binding events by setting the internal reference as 1,000 NPs/unit area with the density factor after measurement (equation 3.3 and Figure 3.8c).

$$\text{normalized binding events} = (\text{binding events})\ \frac{1000\text{NPs/unit area}}{[I-NP]^{0.5}[M-NP]^{0.5}} \quad (3)$$

We calculated the k values for nine different OK-NP reactions with the slope of a linear relation region of the calibration curve (Figure 3.10 and Table 3.2). Considering melting temperature of a target sequence, the association reaction between R-NP and B-NP shows the highest value. The rate constant is affected by the hybridization energy, which is determined by the target miRNA sequence, DNA modification density for OK-NPs, NP morphology, etc. The diversity in k value implies that the target sequence and the types of NPs affects the binding efficiency.

Under these conditions, we obtained the calibration curves of the normalized binding events with target concentrations ranging from 3 pM to 300 pM (Figure 3.9). The binding events were counted on 120 × 120 μm^2

SLBs with consecutive images per 10 min. The logarithm of target concentration showed linear behavior with the normalized binding events (Figure 3.10). The limit of detection (LoD) ranged between 3 pM and 10 pM (30 amol to 100 amol) for 9 miRNA targets without optimizations. The kinetic responses of binding events were dependent on the combination of NPs. Furthermore, miRNA sequence has an influence on the kinetics of assembly and disassembly with complementary DNA sequences.[31]

An assay time of 1 h was sufficient to discriminate different target concentrations. Longer assay time did not noticeably increase the sensitivity because the binding event curve reached a plateau after 1 h when small amount of target present. OK-NLB assay allows for differentiating small difference in miRNA expression, which is key to distinguishing dysregulated miRNA expression for cancer diagnosis.[19]

To examine the multiplexing capability and the cross-reactivity of the OK-NLB assay, we tested samples containing 100 pM of targets with several different combinations of miRNA targets (Figures 3.11a,b). miRNA profiling results were analyzed through in situ monitoring of nine association reactions. Although each M-NP is designed to bind to three types of I-NPs simultaneously, the assay showed negligible cross-reactivity in all the cases, and specifically detected the targets with high reliability and quantification capability. Even when all 9 targets existed in one sample, the assay was able to detect all the targets with the similar quantification results (the far right histogram of Figure 3.11b). We also confirmed the specificity of the assay.
300 pM and 10 pM of single-base-mismatched targets were tested for three

orthogonal targets (miR-21 for MG-IG, miR-155 for MB-IB, and miR-205 for MR-IR; Figure 3.12a and Table 3.3). The single-base-mismatched target showed <43% signal intensities of the signals for 300 pM perfectly matched DNA case. The signals from 10 pM single-basemismatched targets were not differentiable from control signals. The single nucleotide polymorphism (SNP) in G-C pair for miR-205 showed greater discrimination than SNP in A-U pair for miR-21. The detected amount of 300 pM single-base mismatched input was ranged between 10 pM and less than the LoD. The results prove the SNP selectivity and specificity of the OK-NLB assay.

Finally, we performed miRNA profiling of total RNA samples extracted from HeLa cells (human cervical adenocarcinoma) with the OK-NLB assay (Figure 3.12b). We used 0.6 μg of total RNA for cancer cell assay. miR-21, an oncogene widely overexpressed in diverse cancers including cervical cancers,[32] showed the highest expression level. The measured values of miR-141, miR-146a, miR-155, and miR-205 were below LoD, and this result is consistent with the previous report that showed those miRNAs have low or no expression in HeLa cells.[33] We spiked miR-146a (30 pM final concentration) in a total RNA sample and quantified it using the OK-NLB assay. The detected amount of target was 25.7 ± 1.62 pM. The spiked sample showed 94% of the normalized binding events, compared to that of the same concentration of target sample in buffer condition. 6 % signal loss was largely due to cell debris in the lysate observed on the SLB (Figure 3.13). We further validated the result of the OK-NLB assay using qRT-PCR. The relative expression value of each miRNA to the internal reference U6

was plotted against the absolute concentration of miRNA obtained from OK-NLB assay (Figure 3.12c). The two assay results showed strong agreement with R^2 values of >0.999. Moreover, the expression pattern of 9 miRNA targets was well matched with the reported value obtained by microarraybased assay.[34]

3.4. Conclusion

In summary, we developed the optokinetically encoded light-scattering NP-based assay on SLB (OK-NLB assay), which allows real-time monitoring of individual NP assembly modes. The assay enables rapid, sensitive, quantitative and multiplexed profiling of 9 different miRNAs in one sample without complicated setup, target modification and enzymatic amplification. The probes on SLB used herein were modified with three different target miRNA complements and mobility-controlling biotinylated DNA for multiplexed optokinetic encoding, and showed remarkable photostability with DFM that allows for in situ monitoring of the probes and reliable quantification of their binding events with miRNA. As a proof of concept, we showed the highly specific detection of various combinations of 9 different miRNA targets with 9 interacting pairs of probes between mobile R, G or B probes and immobile R, G or B probes on SLB. In situ single-particle monitoring and normalized RGB analysis of 2D diffusion and target miRNA-facilitated binding of a large number of the photostable NPs with DFM in a highly parallel manner allows for reliably differentiating and quantifying 9 different miRNA targets in one sample. Moreover, single-base mismatched target miRNA sequences were clearly discernible from target miRNA sequences on the OK-NLB assay platform. Highly selective detection of different miRNA sequences used here implies the diagnosis of breast, prostate, lung, pancreas and stomach cancers from clinical samples could be potentially possible with further optimizations.[15] For rigorous validation, we

profiled the expression levels of 9 miRNAs from cervical cancer cell extracts within 1 h and confirmed that the expression pattern is consistent with qRT-PCR result. The assay should be readily applicable to study other complex biological and chemical reactions because the surface of OK-NPs can be modified with diverse biochemical ligands.[34−36] The multiplexed profiling strategy with OK-NPs on SLB expands the number of multiplexable targets and open new ways of developing highly multiplexed signals with photostable probes on a highly analyzable, quantifiable platform. The OK-NLB platform could be useful for rapid and multiplexed pathogen detection,[37,38] as well as cancer diagnosis.

Methods of using SLB and nanoscale structures can also be used to identify the interaction of various substances, such as DNA and RNA, as well as proteins and proteins. The study of interactions between molecules and particles will help to understand the numerous chemical and biological principles. The method used here is very useful because it can track a large number of individual particles in high resolution in real time, and will provide information and insight on important scientific principles that have not been known.

3.5. References

1. Kuzyk, A.; Schreiber, R.; Fan, Z.; Pardatscher, G.; Roller, E.; Högele, A.; Simmel, F. C.; Govorov, A. O.; Liedl, T. *Nature* 2012, *483*, 311.

2. Li, D.; Nielsen, M. H.; Lee, J. R. I.; Frandsen, C.; Banfield, J. F.; Yoreo, J. J. D. *Science* 2012, *336*, 1014.

3. Liu, Y.; Lin, X.-M.; Sun, Y.; Rajh, T. *J. Am. Chem. Soc.* 2013, *135*, 3764.

4. Langille, M. R.; Zhang, J.; Personick, M. L.; Li, S.; Mirkin, C. A. *Science* 2012, *337*, 954.

5. Joo, C.; Balci, H.; Ishitsuka, Y.; Buranachai, C.; Ha, T. *Annu. Rev. Biochem.* 2008, *77*, 51.

6. Yu, J.; Wu, C.; Sahu, S. P.; Fernando, L. P.; Szymanski, C.; McNeill, J. *J. Am. Chem. Soc.* 2012, *131*, 18410.

7. Milo, R.; Shen-Orr, S.; Itzkovitz, S.; Kashtan, N.; Chklovskii, D.; Alon, U. *Science* 2002, *298*, 824-827.

8. Bray, D. *J. Theor. Biol.* 1990, *143*, 215-231.

9. Grzybowski, B. A.; Bishop, K. J. M.; Kowalczyk, B.; Wilmer, C. E. *Nat. Chem.* 2009, *1*, 31-36.

10. Carregal-romero, S.; Caballero-Díaz, E.; Beqa, L.; Abdelmonem, A. M.; Ochs, M.; Hu.hn, D.; Suau, B. S.; Valcarcel, M.; Parak, W. J. *Annu. Rev. Anal. Chem.* 2013, *6*, 53-81.

11. Zhao, Y.; Cheng, Y.; Shang, L.; Wang, J.; Xie, Z.; Gu, Z. *Small* 2015, *11*, 151-174.

12. He, L.; Hannon, G. J. *Nat. Rev. Genet.* 2004, *5*, 522-531.

13. Mitchell, P. S.; Parkin, R. K.; Kroh, E. M.; Fritz, B. R.; Wyman, S. K.; Pogosova-Agadjanyan, E. L.; Peterson, A.; Noteboom, J.; O'Briant, K. C.; Allen, A.; Lin, D. W.; Urban, N.; Drescher, C. W.; Knudsen, B. S.; Stirewalt, D. L.; Gentleman, R.; Vessella, R. L.; Nelson, P. S.; Martin, D. B.; Tewari, M. *Proc. Natl. Acad. Sci. U. S. A.* 2008, *105*, 10513-10518.

14. Li, Y.; Kowdley, K. V. *Genomics, Proteomics Bioinf.* 2012, *10*, 246-253.

15. Wang, J.; Zhang, K. Y.; Liu, S. M.; Sen, S. *Molecules* 2014, *19*, 1912-1938.

16. Carthew, R. W.; Sontheimer, E. J. *Cell* 2009, *136*, 642-655.

17. Pritchard, C. C.; Cheng, H. H.; Tewari, M. *Nat. Rev. Genet.* 2012, *13*, 358-369.

18. Lee, H.; Park, J.-E.; Nam, J.-M. *Nat. Commun.* 2014, *5*, 3367.

19. Wang, Y.; Zheng, D.; Tan, Q.; Wang, M. X.; Gu, L.-Q. *Nat. Nanotechnol.* 2011, *6*, 668-674.

20. Degliangeli, F.; Kshirsagar, P.; Brunetti, V.; Pompa, P. P.; Fiammengo, R. *J. Am. Chem. Soc.* 2014, *136*, 2264-2267.

21. Alhasan, A. H.; Kim, D. Y.; Daniel, W. L.; Watson, E.; Meeks, J. J.; Thaxton, C. S.; Mirkin, C. A. *Anal. Chem.* 2012, *84*, 4153-4160.

22. Lu, N.; Gao, A.; Dai, P.; Song, S.; Fan, C.; Wang, Y.; Li, T. *Small* 2014, *10*, 2022-2028.

23. Dong, H.; Zhang, J.; Ju, H.; Lu, H.; Wang, S.; Jin, S.; Hao, K.; Du, H.; Zhang, X. *Anal. Chem.* 2012, *84*, 4587-4593.

24. Zeng, Y.; Zhu, G.; Yang, X.; Cao, J.; Jing, Z.; Zhang, C. *Chem. Commun.* 2014, *50*, 7160-7162.

25. Lee, Y. K.; Kim, S.; Oh, J. W.; Nam, J. M. *J. Am. Chem. Soc.* 2014, *136*, 4081.4088.

26. Volinia, S.; Calin, G. a; Liu, C.-G.; Ambs, S.; Cimmino, A.; Petrocca, F.; Visone, R.; Iorio, M.; Roldo, C.; Ferracin, M.; Prueitt, R. L.; Yanaihara, N.; Lanza, G.; Scarpa, A.; Vecchione, A.; Negrini, M.; Harris, C. C.; Croce, C. M. *Proc. Natl. Acad. Sci. U. S. A.* 2006, *103*, 2257-2261.

27. Wang, W.-T.; Chen, Y.-Q. J. *J. Hematol. Oncol.* 2014, *7*, 86.

28. Kosaka, N.; Iguchi, H.; Ochiya, T. *Cancer Sci.* 2010, *101*, 2087-2092.

29. Hsieh, C. L.; Spindler, S.; Ehrig, J.; Sandoghdar, V. *J. Phys. Chem. B* 2014, *118*, 1545-1554.

30. Rong, G.; Wang, H.; Skewis, L. R.; Reinhard, B. M. *Nano Lett.* 2008, *8*, 3386-3393.

31. Johnson-Buck, A.; Su, X.; Giraldez, M. D.; Zhao, M.; Tewari, M.; Walter, N. G. *Nat. Biotechnol.* 2015, *33*, 730.

32. Lu, Z.; Liu, M.; Stribinskis, V.; Klinge, C. M.; Ramos, K. S.; Colburn, N. H.; Li, Y. *Oncogene* 2008, *27*, 4373-4379.

33. Nelson, P. T.; Baldwin, D. A.; Scearce, L. M.; Oberholtzer, J. C.; Tobias, J. W.; Mourelatos, Z. *Nat. Methods* 2004, *1*, 155.161.

34. Xianyu, Y.; Xie, Y.; Wang, N.; Wang, Z.; Jiang, X. *Small* 2015, *11*, 5510-5514.

35. Chen, W.; Cao, F.; Zheng, W.; Tian, Y.; Xianyu, Y.; Xu, P.; Zhang, W.; Wang, Z.; Deng, K.; Jiang, X. *Nanoscale* 2015, *7*, 2042-2049.

36. Zhou, W.; Gao, X.; Liu, D.; Chen, X. *Chem. Rev.* 2015, *115*, 10575-10636.

37. Hauck, T. S.; Giri, S.; Gao, Y.; Chan, W. C. W. *Adv. Drug Delivery Rev.*

2010, *62*, 438-448.

38. Hu, R.; Liu, T.; Zhang, X. B.; Huan, S. Y.; Wu, C.; Fu, T.; Tan, W. *Anal. Chem.* 2014, *86*, 5009-5016.

Figures and Tables

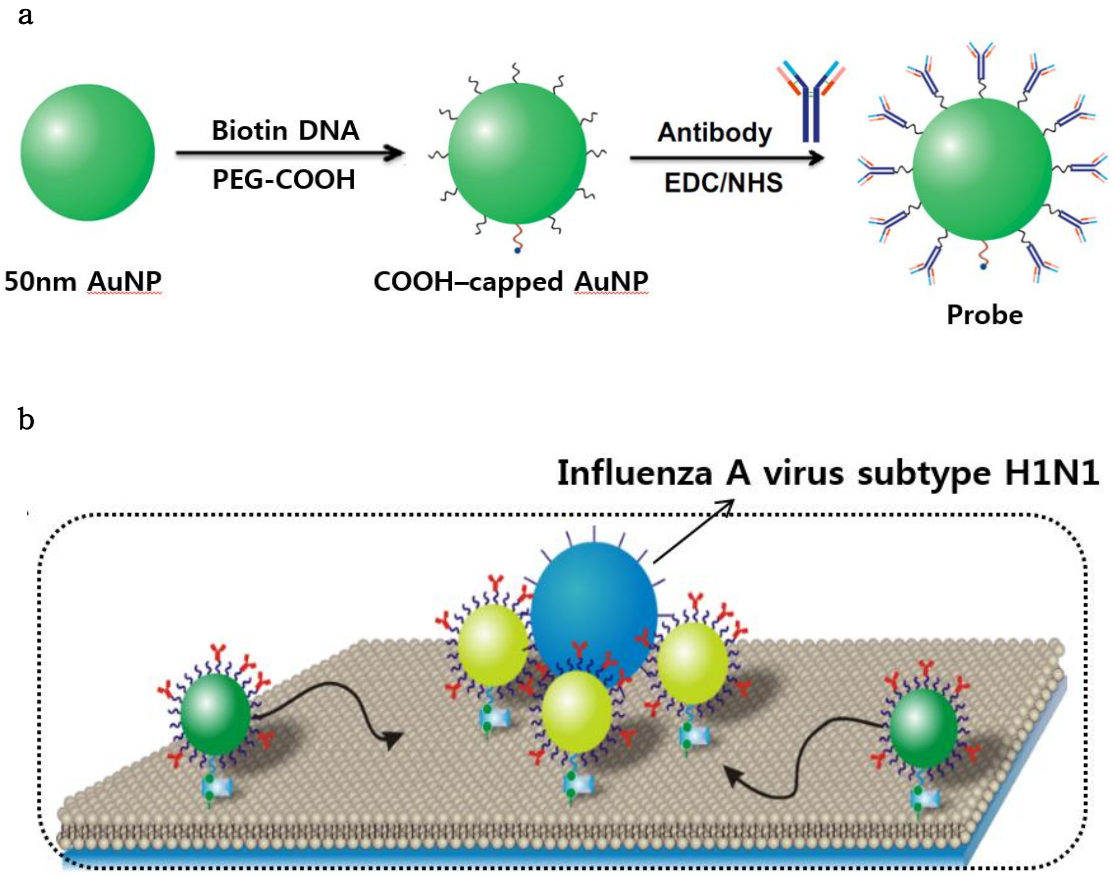

Figure 1.1. Dark Field-Nanoprobes on Supported Lipid Bilayer(DF-NLB) system. (a) Synthetic procedure of antibody modified gold nanoparticle(probe). (b) The nanoparticles connected to the SLB by biotin-streptavidin interaction move together as the lipid moves. In the presence of target virus, nanoparticles that are freely diffusing on the SLB surface can be bound via the virus. In this case, the nanoparticles maintain a close distance and the near-field interaction continues.

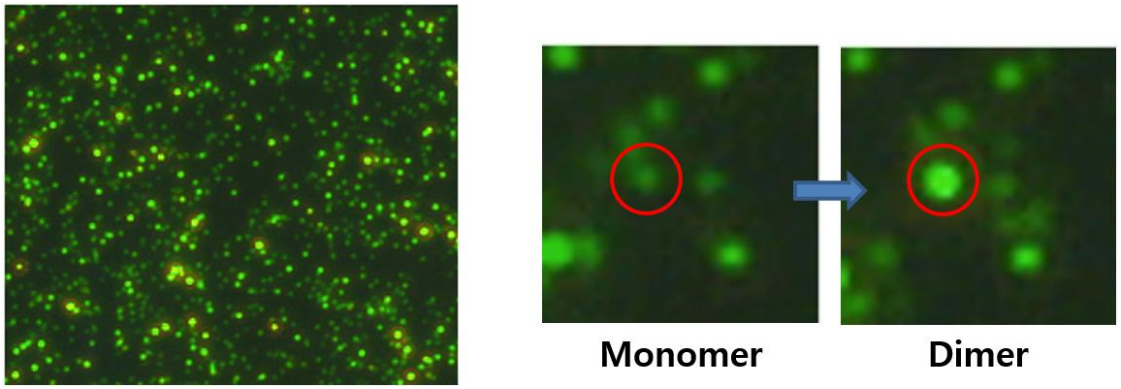

Figure 1.2. DF-NLB based target virus(Influenza A virus subtype H1N1) detection. In the red circle on the right, the scattering intensity increases as the probe forms a dimer by the target virus.

a

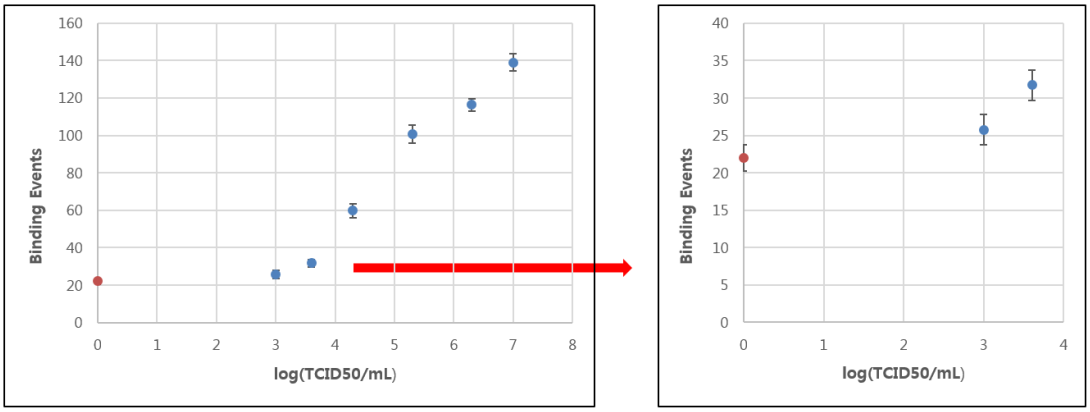

b

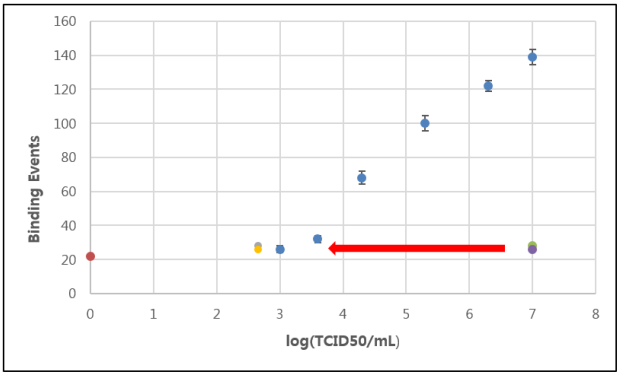

Figure 1.3. Calibration curves between the binding event and the virus concentration was obtained using various concentrations of virus samples. As the amount of target virus increased, the number of bound nanoparticles increased at the same time. (a) In the current system, detection was possible up to about 1000 $TCID_{50}$/mL for target virus. (b) The number of nanoparticles bound(binding event) by a high concentration of non-target virus was lower than that of target virus 1000 $TCID_{50}$/mL.

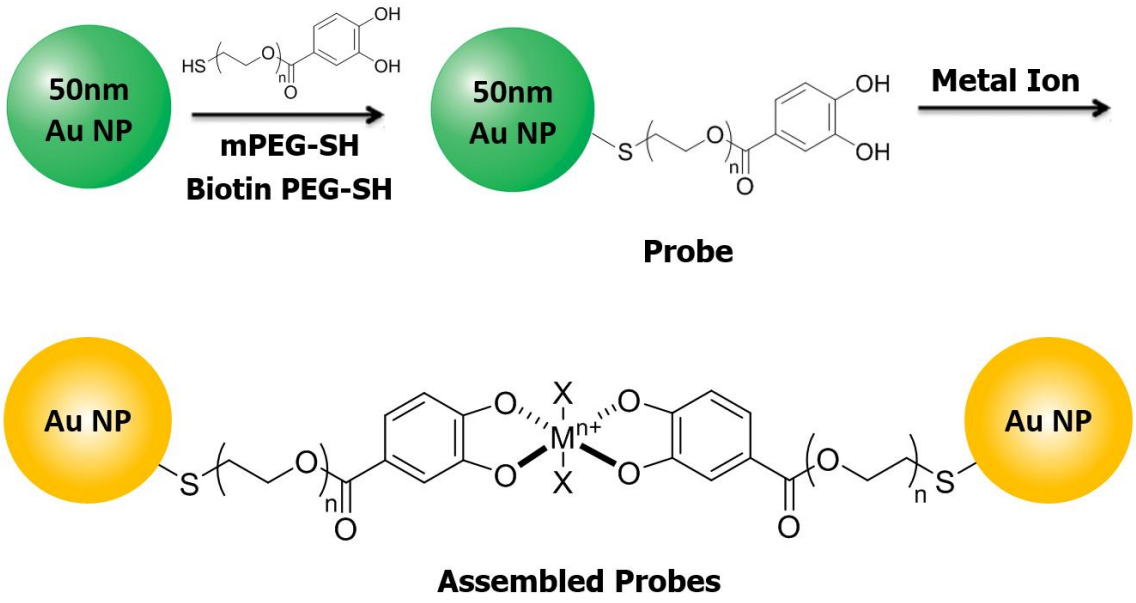

Figure 2.1. Synthetic procedure of ligand-modified gold nanoparticle(probe). Catechol ligands are suitable for controlling AuNP assembly using external stimuli such as pH, redox reagent and Fe^{3+}.

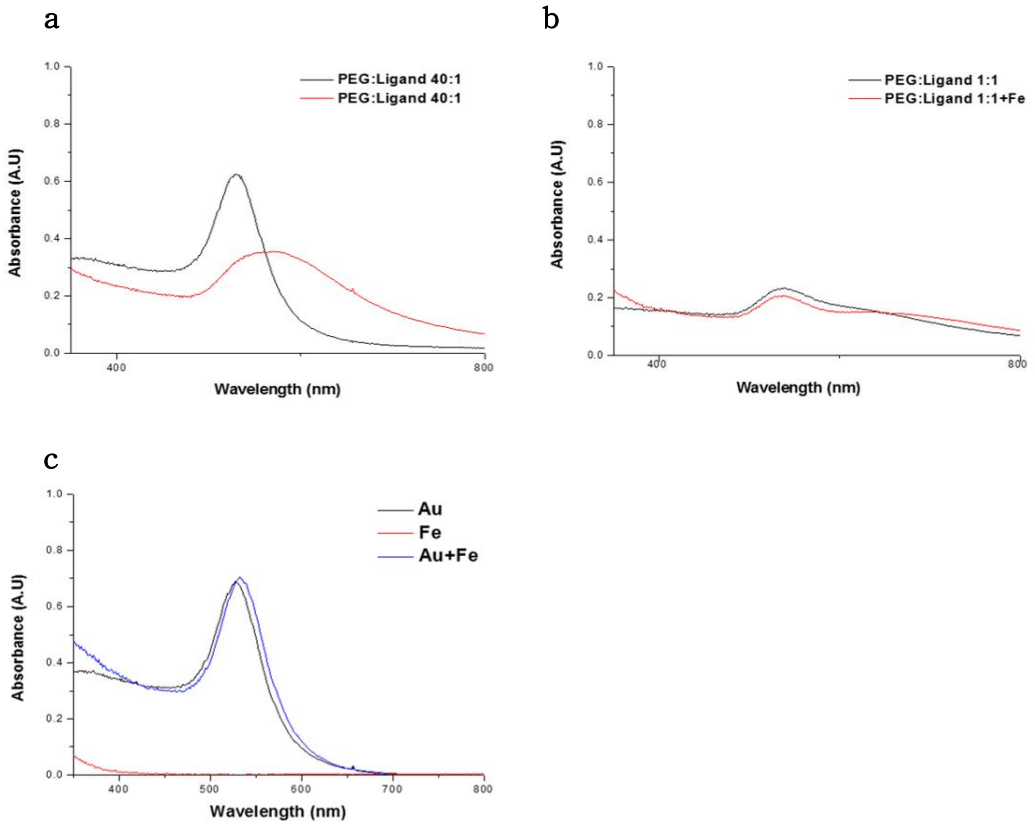

Figure 2.2. UV-Vis data of Fe^{3+}-induced assembly in solution phase. The surface of gold nanoparticles was modified by varying the ratio of 1k thiol-mPEG to ligand, and whether catechol ligands specifically bound Fe^{3+} in solution was analyzed by UV-Vis analysis. (a) When gold nanoparticles were modified with the ratio of ligand to PEG of 1: 1 and Fe^{3+} was added, a new peak appeared at a wavelength of 560 nm where the absorbance peak decreased to about 650 nm. (b) In addition, when the ligand and PEG were introduced into the gold nanoparticles at a ratio of 1:40, the peak around 560 nm became wider and redshift when Fe^{3+} was added. (c) The UV spectra of gold nanoparticles, gold nanoparticles + Fe^{3+}, and Fe^{3+} were measured to see if there was a change in the UV spectrum due to nonspecific reaction between nanoparticles and Fe^{3+}.

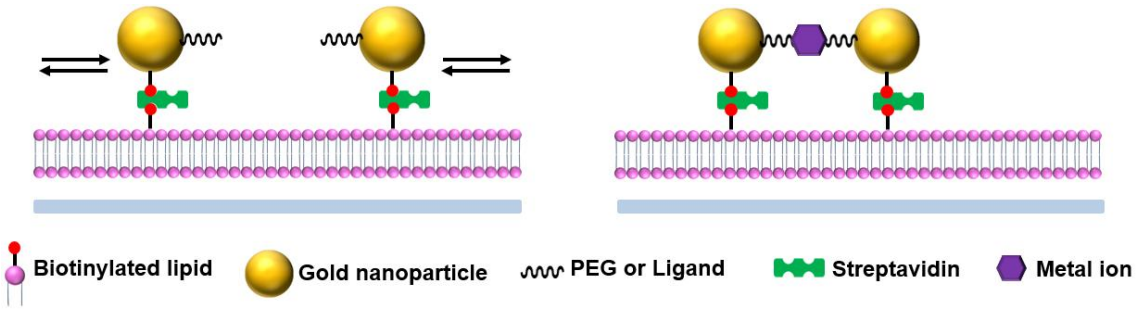

Figure 2.3. Dark Field-Nanoprobes on Supported Lipid Bilayer(DF-NLB) system. The nanoparticles connected to the SLB by biotin-streptavidin interaction move together as the lipid moves. In the presence of metal ion, nanoparticles that are freely diffusing on the SLB surface can be bound via metal ion.

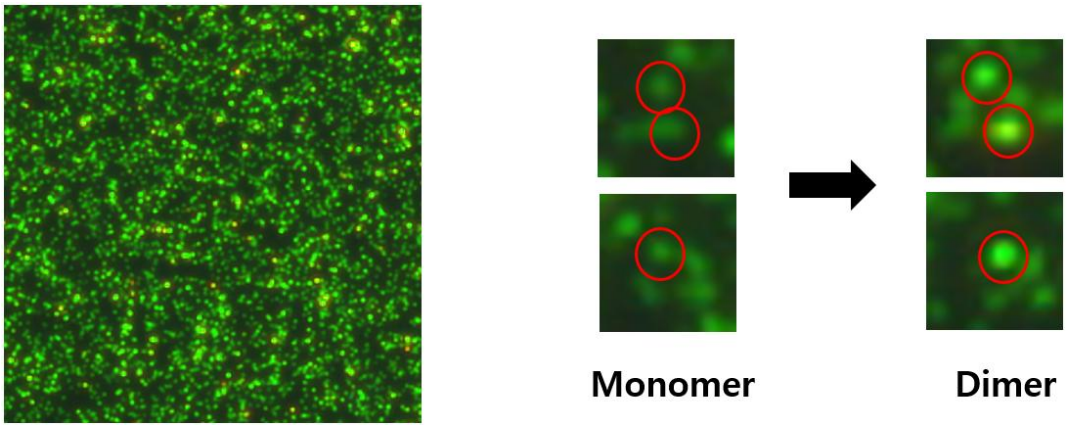

Figure 2.4. Fe^{3+}-induced assembly of the ligand-modified nanoparticles on SLB. In the red circle on the right, the scattering intensity increases as the probe forms a dimer by the Fe^{3+} ion.

Concentration of Fe^{3+}	Assembly event
Control ($[Cu^{2+}]$ = 100 nM)	21
500 pM	76
100 nM	169

Table 2.1. The number of assembly event of 30 min Fe^{3+}-induced assembly case.

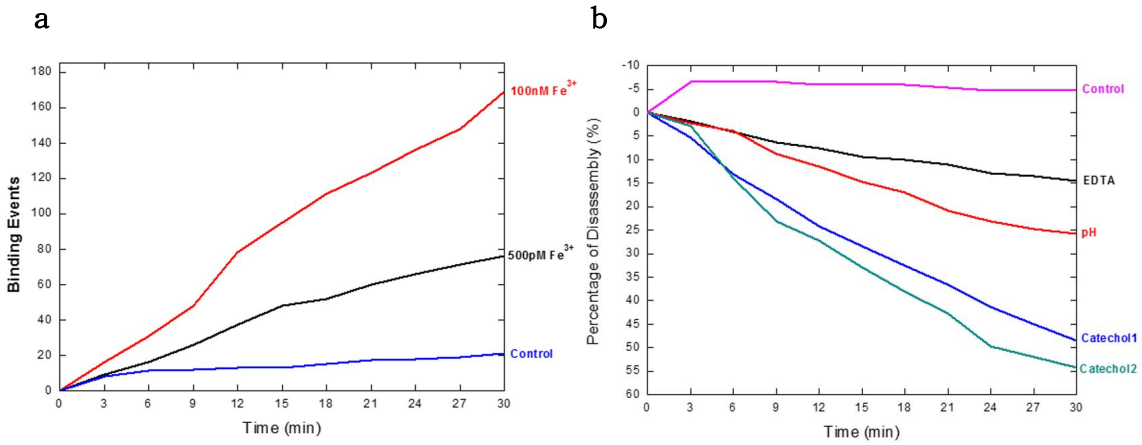

Figure 2.5. Fe^{3+}-induced assembly of the ligand-modified nanoparticles on SLB. (a) The binding between the nanoparticles via the Fe^{3+}-induced assembly was clearly distinguished by comparison with the control group through observation for 30 minutes. (b) The Fe^{3+}-induced assembly on the SLB was disassembled by three methods: pH change, EDTA addition, and excess free catechol addition. The pH change changes the chemical properties of catechol and reduces the binding force with Fe^{3+}. EDTA and excess free catechol have the effect of removing Fe^{3+} by binding to Fe^{3+} used in the assembly. Among the three methods, the free chatechol method was most effective.

a

b

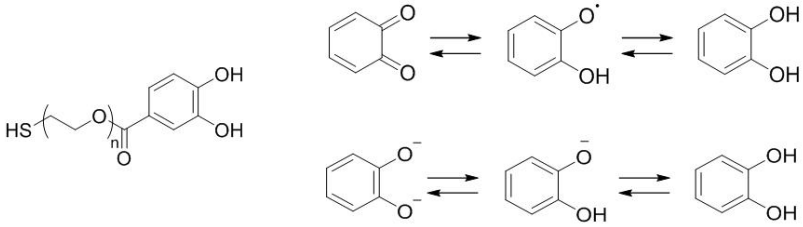

c

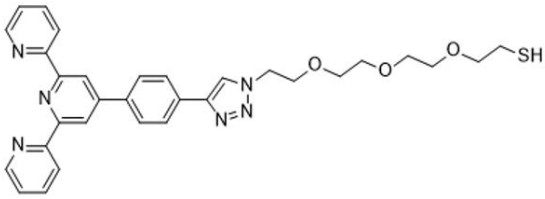

Figure 2.6. (a) A "synthetic pathway" for easy synthesis of various ligands. This method is convenient because it allows introduction of various ligands at the end of the synthesis with click chemistry. (b) Redox active and pH sensitive catechol ligand. (c) Terpy ligand.

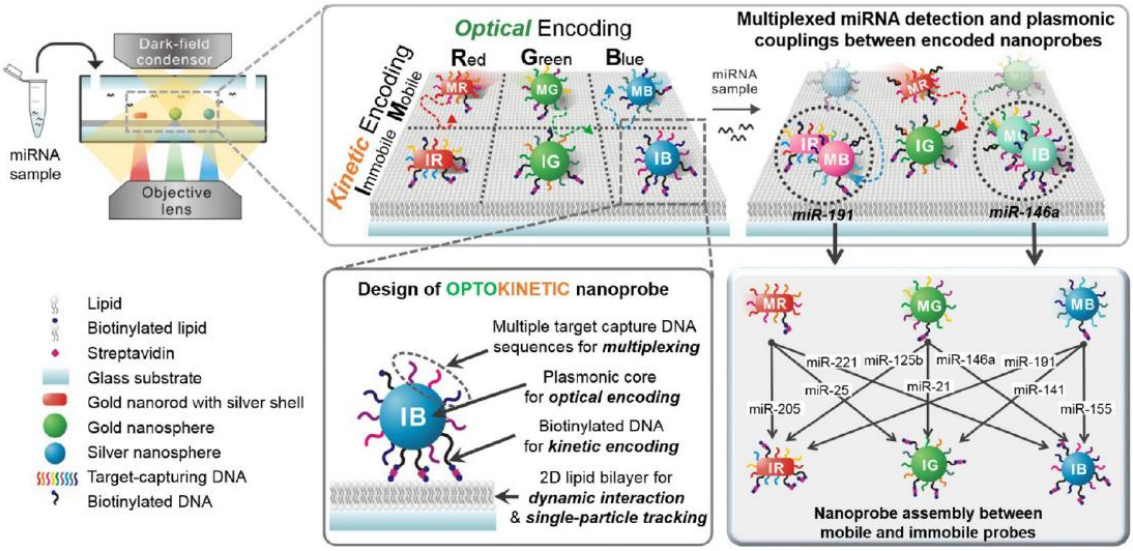

Figure 3.1. Optokinetically encoded nanoprobe (OK-NP)-tethered supported lipid bilayer (SLB) assay (OK-NLB assay). The miRNA sample is directly injected into a reaction chamber, and NP interactions are monitored with dark-field microscopy (DFM). Six types of OK-NPs are prepared by kinetic [mobile (M) and immobile (I)] and optical [red (R), green (G), and blue (B)] coding methods. OK-NPs are composed of plasmonic nanoparticle core, multiple target capture DNAs, and biotinylated DNA. The NP assembly events between the M-NPs and the I-NPs are mediated by target miRNAs and identified with scattering color changes via plasmonic coupling. The nineplexing strategy using combinatorial assemblies between OK-NPs relies on each assembly mode, which was mediated by 9 different target miRNAs (bottom right).

a

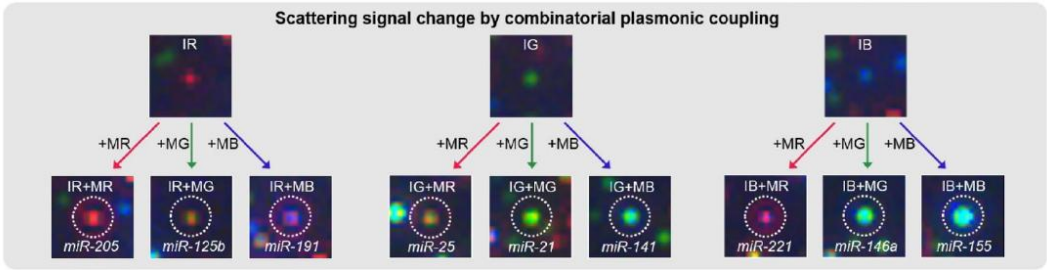

b

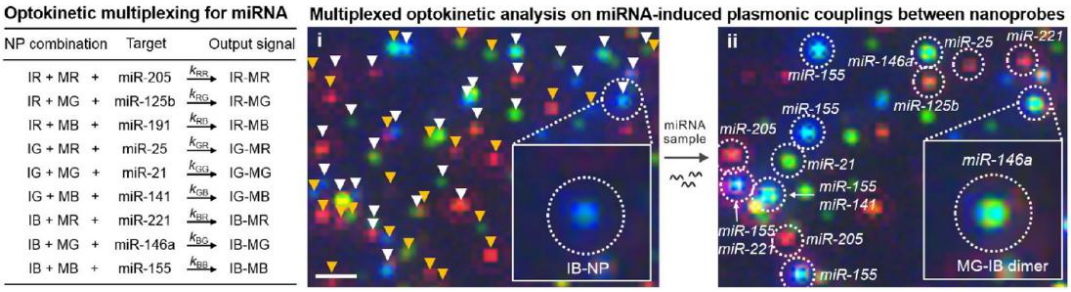

Figure 3.2. (a) Nine different scattering signal changes due to combinatorial plasmonic couplings induced by M-NPs binding to I-NPs. (b) Nine NP assembly reaction equations are described as multicomponent association reactions. (c) DFM images of DF scattering signals from individual OK-NPs on SLB. (c) (i) OK-NP identification by particle color and mobility. White and orange solid triangles indicate I-NPs and M-NPs, respectively. (ii) Multiplexed combinations of OK-NP assemblies reveal the target miRNA-induced particle assemblies in highly parallel manner (white dashed circles). The scale bar is 2 μm.

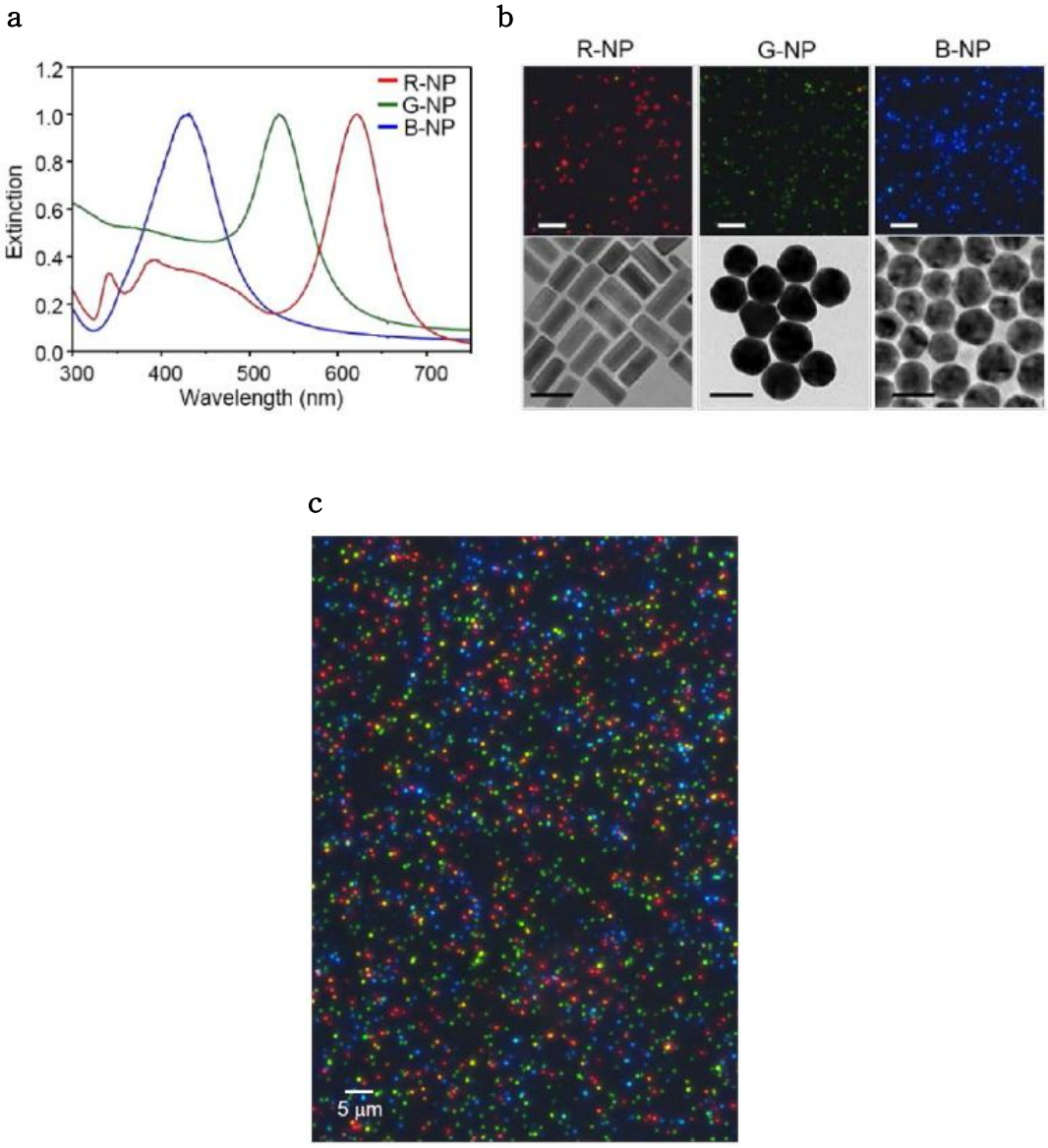

Figure 3.3. Photostable plasmonic NPs and DFM-based identification of the types of OK-NPs. (a) The extinction spectra of three optically encoded NPs. (b) DFM images (top) and transmission electron microscopy images (bottom) of R-NPs, G-NPs, and B-NPs (from left to right). The scale bars are 10 μm (DFM) and 50 nm (TEM). (c) A large area DFM image of the OK-NPs on SLB.

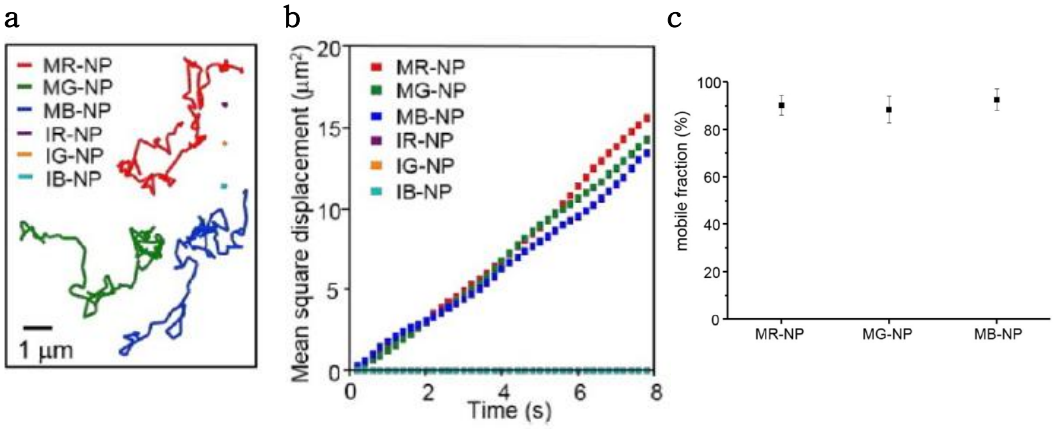

Figure 3.4. (a) Representative diffusion trajectories and (b) mean square displacement plot of OK-NPs. The NPs with two kinetic states (M-NPs and I-NPs) show clear distinction in diffusion. (c) Mobile fractions of MR-, MG-, and MB-NPs. Each standard deviation was obtained from three independent measurements (N=500).

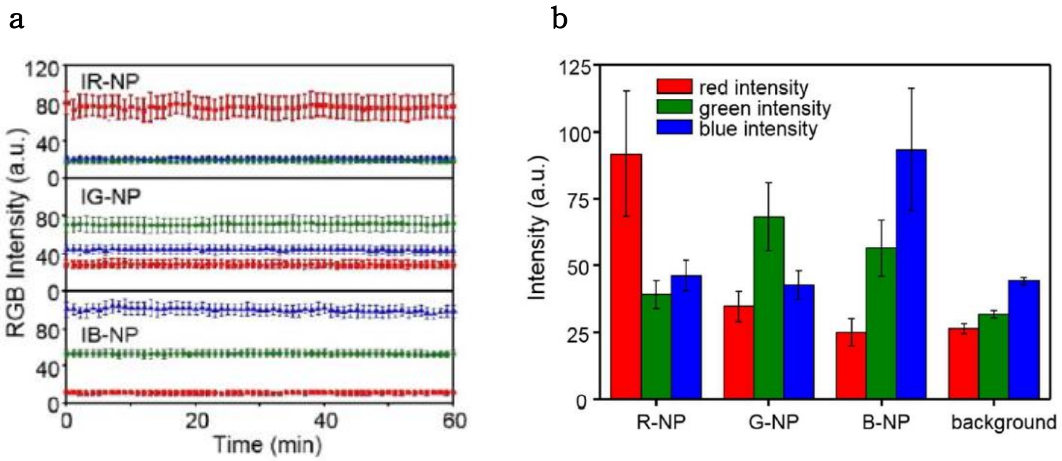

Figure 3.5. (a) Averaged red (red square), green (green circle), and blue (blue triangle) scattering intensity of each I-NP under continuous dark-field illumination for 60 min. The images were taken every 1 min, and error bars are standard deviation from 20 NPs. (b) Average RGB intensities of R-, G-, and B-NPs and background signals (N=100).

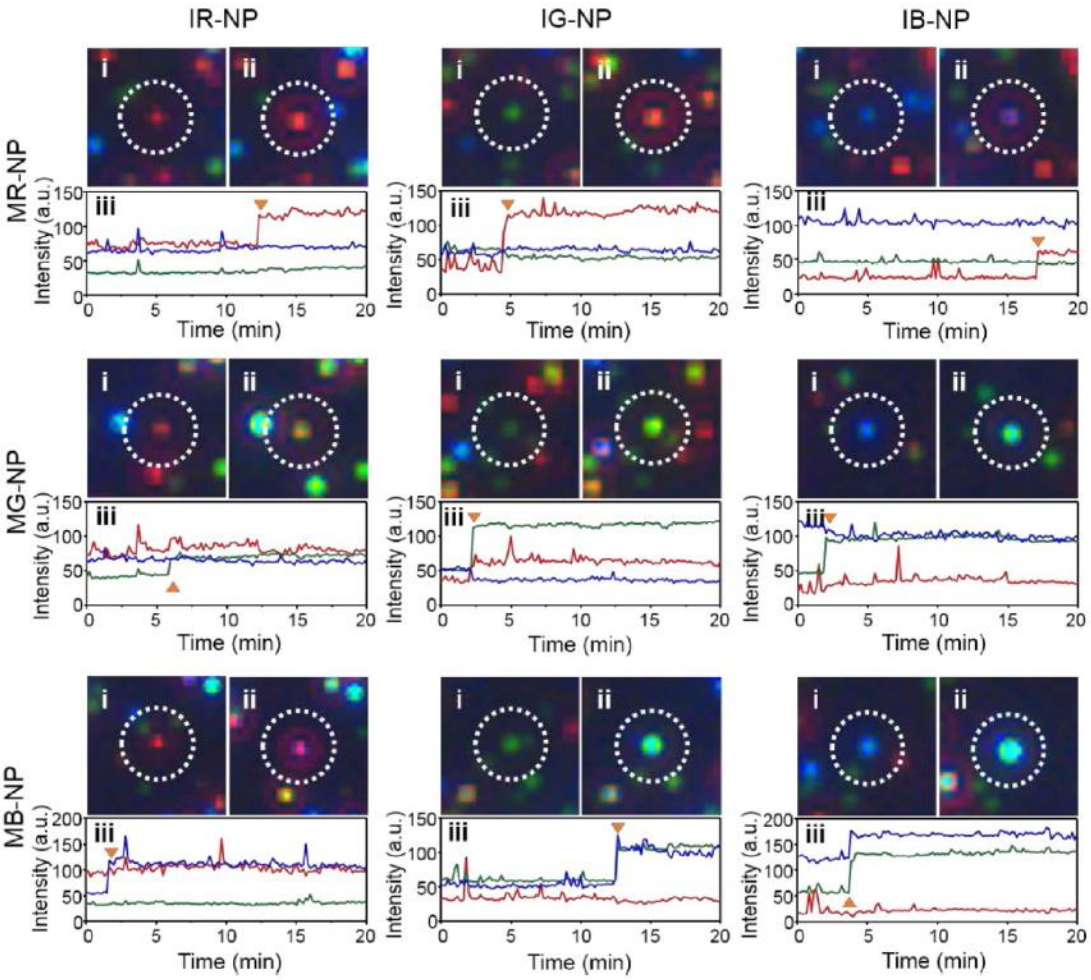

Figure 3.6. Multiplexable and parallel identification of the interaction between OK-NPs by combinatorial plasmonic coupling. Real-time monitoring of combinatorial assemblies between OK-NPs. OK-NPs were monitored with 10 s interval after addition of 10 nM of 9 target miRNAs. DFM images of 9 combinations at (i) 0 min and (ii) 20 min. The bindings of M-NPs to I-NPs result in distinct color and signal intensity change. (iii) The RGB intensity profiles show characteristic patterns for the binding of MR-, MG-, and MB-NPs. The binding events are indicated with orange triangles.

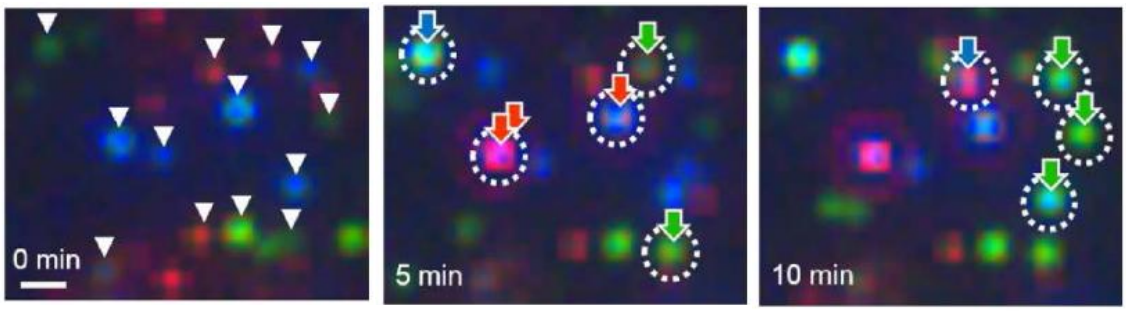

Figure 3.7. Parallel observation of the individual binding events (white dashed circle) between I-NPs (white triangle) and MR- (red arrow), MG- (green arrow), and MB-NPs (blue arrow). The scale bar is 1 μm.

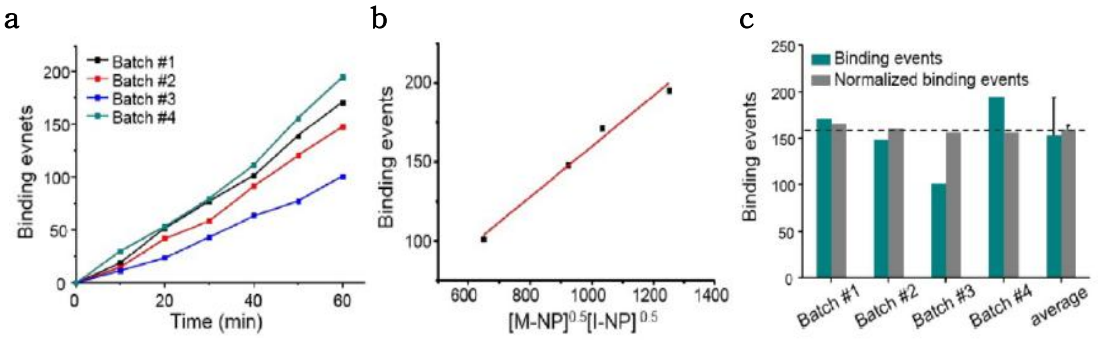

Figure 3.8. Kinetics and quantification of miRNA binding events. (a) Cumulative binding events for 60 min between MR-NPs and IB-NPs at 100 pM miRNA with different NP densities on SLB. (b) The number of binding events at 60 min is proportional to $[M-NP]^{0.5}$ and $[I-NP]^{0.5}$. The orders were fitted to have the largest R^2 value (0.9868) and the smallest standard deviation of normalized binding events. (c) Binding events at 60 min from different batches were normalized by (normalized binding events) = $\frac{(\text{binding event})}{[M-NP]^{0.5}[I-NP]^{0.5}}$ × 1000NPs/unit area was set as an internal reference. The normalized binding events with varying NP densities show similar values with a small standard deviation compared to the standard deviation without normalization.

	Batch #1	Batch #2	Batch #3	Batch #4
# of I-NPs/unit area ([M-NP])	1629	1440	882	1872
# of M-NPs/unit area ([I-NP])	657	594	477	837
Binding events	171	148	101	195

Table 3.1. Binding events of 100 pM of target miRNA after 60 min from four batches with different particle densities on SLB. The ratios of I-NPs to M-NPs ranged between 1.8 and 2.5 to minimize multimer (trimer or higher) formation. Unit area is 120 × 120 μm^2.

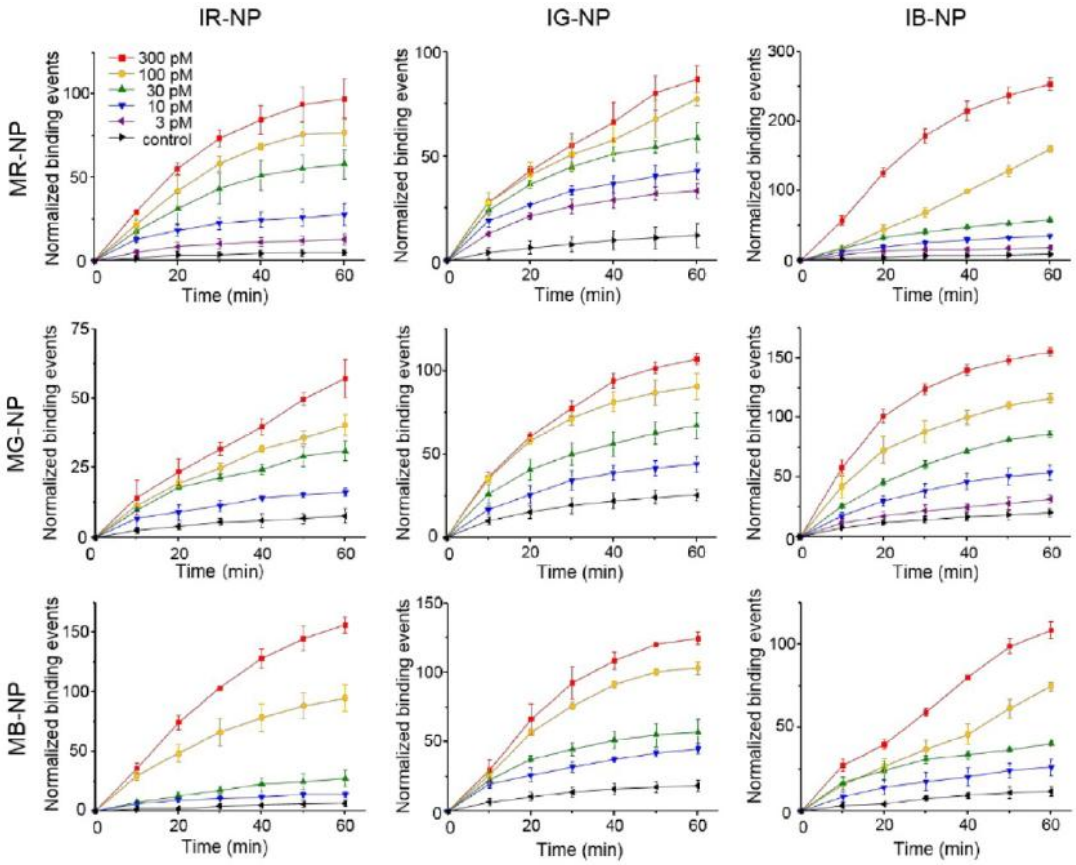

Figure 3.9. Normalized binding events of 9 miRNAs at different concentrations. The error bars represent the standard deviations from three independent experiments. Control experiments contained 300 pM of negative control miRNA (miR-100).

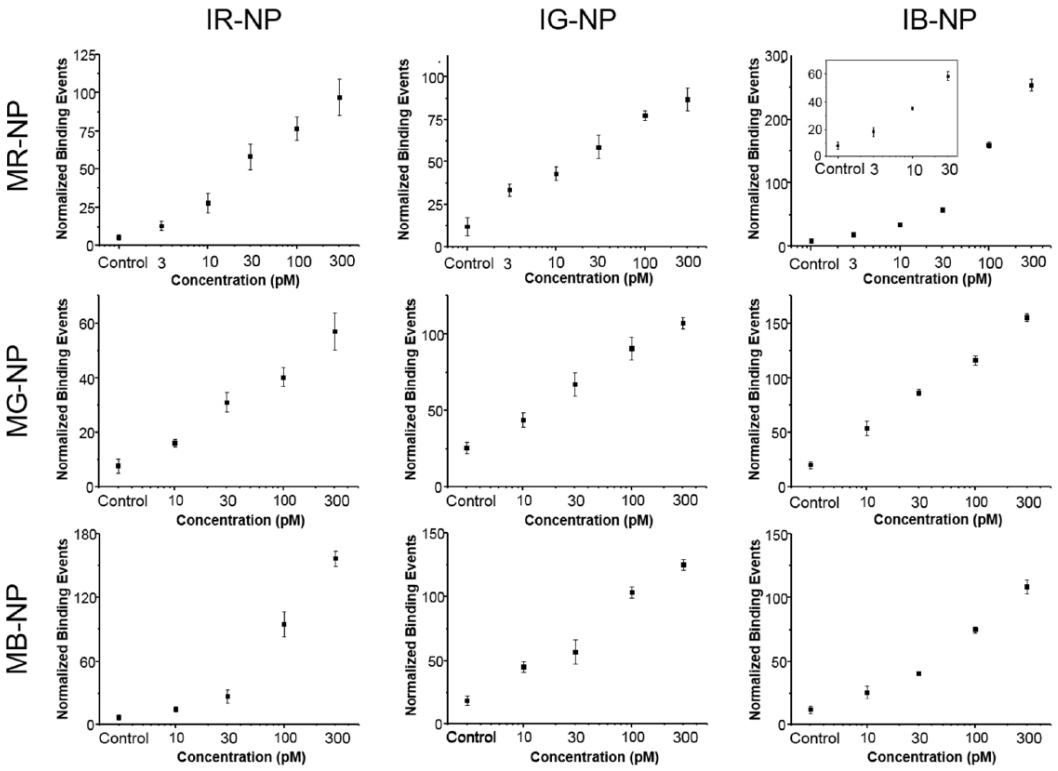

Figure 3.10. Calibration curves with varying target concentrations. The error bars represent the standard deviations from three independent experiments. Control experiments contained 300 pM of negative control miRNA (miR-100).

	IR-NP	IG-NP	IB-NP
MR-NP	45.6	30.4	195.4
MG-NP	26.5	43.0	67.5
MB-NP	129.1	54.1	67.6

Table 3.2. Reaction constants for each combinatorial assembly reaction.

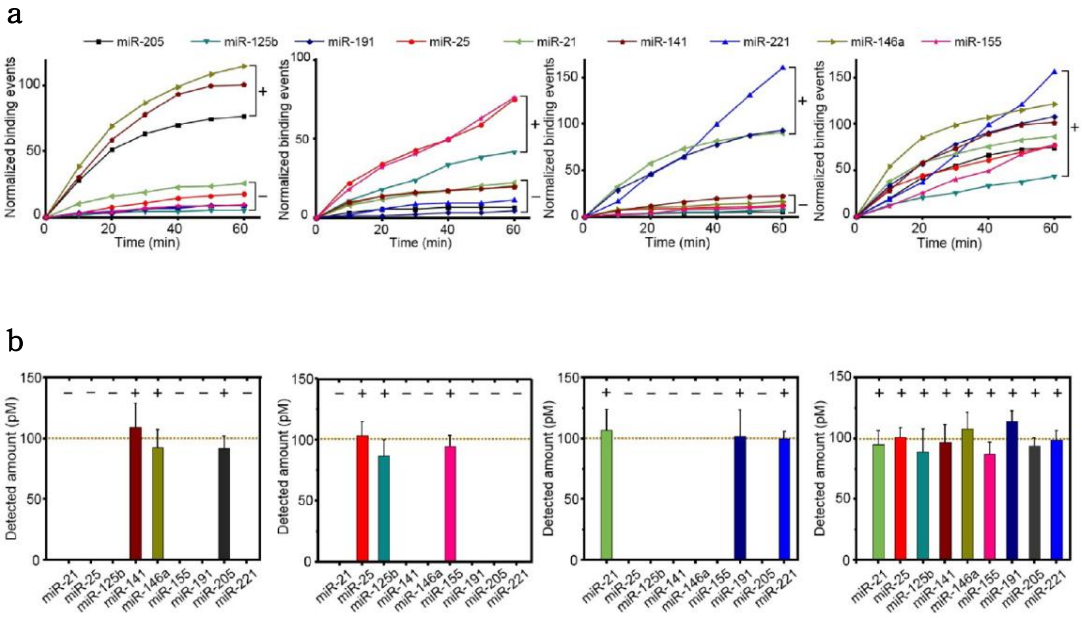

Figure 3.11. Multiplexed detection of miRNA sequences. (a) Representative data for in situ monitoring of binding events and (b) multiplexed profiling results from different combinations of 100 pM target miRNA sequences. Plus (minus) sign indicates presence (absence) of the target miRNA in samples. The detected amount was obtained from calibration curves. The dashed lines indicate the added amount of target miRNA. The results prove the multiplexing capability and negligible cross-reactivity within experimental errors of the assay.

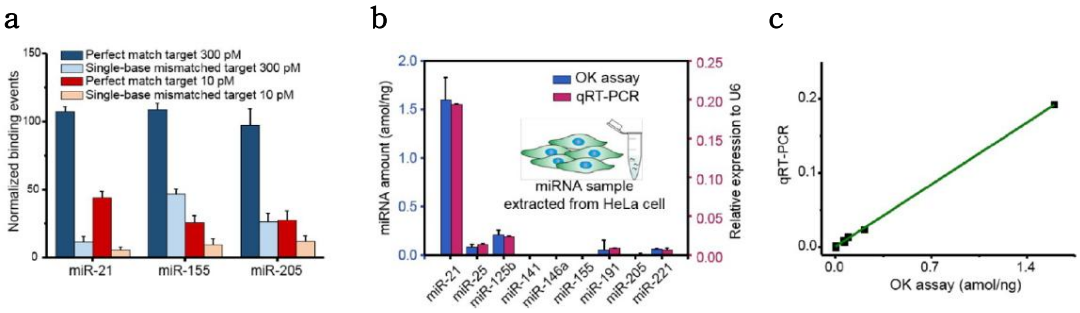

Figure 3.12. (a) Discrimination between target miRNA and single-base-mismatched target at 300 and 10 pM. Single-base-mismatched target shows <43% normalized binding events at 300 pM and indistinguishable signals from control signals at 10 pM. (b) Multiplexed miRNA profiling of total RNA extract from HeLa cells and validation with qRT-PCR. qRT-PCR result shows relative expression value to U6 snRNA. (c) Correlation of OK-NLB assay with qRT-PCR based on the results of total RNA from HeLa cells. The 9 target miRNA results obtained with two methods show a strong agreement (R^2 = 0.9993). The standard deviations are obtained from three independent experiments.

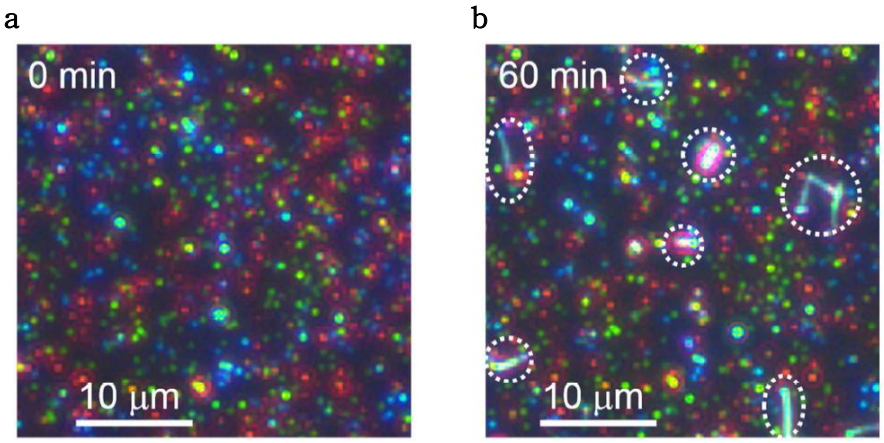

Figure 3.13. Cell debris from total RNA extract sample on NP-modified SLB (white dashed circles). Nonspecific binding of NPs to cell debris induces signal loss.

Table 3.3. Oligonucleotide and miRNA sequences.

Synthetic oligonucleotides and miRNAs	Sequences (5' → 3')
miR-21	UAGCUUAUCAGACUGAUGUUGA
miR-25	CAUUGCACUUGUCUCGGUCUGA
miR-125b	UCCCUGAGACCCUAACUUGUGA
miR-141	UAACACUGUCUGGUAAAGAUGG
miR-146a	UGAGAACUGAAUUCCAUGGGUU
miR-155	UUAAUGCUAAUCGUGAUAGGGGU
miR-191	CAACGGAAUCCCAAAAGCAGCUG
miR-205	UCCUUCAUUCCACCGGAGUCUG
miR-221	AGCUACAUUGUCUGCUGGGUUUC
miR-100	AACCCGUAGAUCCGAACUUGUG
Single base mismatched miR-21	UAGCAUAUCAGACUGAUGUUGA
Single base mismatched miR-155	UUAAUGCUGAUCGUGAUAGGGGU
Single base mismatched miR-205	UCCUUCAUUCCACCGGAAUCUG
biotinylated DNA for M-NP	HS-$(CH_2)_6$-PEG_6-CTTTGAGCACTGTTAGCGTGTGTGGAATTTTAAT-biotin
biotinylated DNA for I-NP	biotin-TAATTTTAAGGTGTGTGCGATTGTCACGAGTTTC-PEG_6-$(CH_2)_3$-SH
miR-205 capturing DNA for MR-NP	HS-$(CH_2)_6$-A_{15}-PEG_6-CAGACTCCGGT
miR-25 capturing DNA for MR-NP	HS-$(CH_2)_6$-A_{15}-PEG_6-TCAGACCGAGA
miR-221 capturing DNA for MR-NP	HS-$(CH_2)_6$-A_{15}-PEG_6-GAAACCCAGCA
miR-125b capturing DNA for MG-NP	HS-$(CH_2)_6$-A_{15}-PEG_6-TCACAAGTTAG

miR-21 capturing DNA for MG-NP	HS-$(CH_2)_6$-A_{15}-PEG_6-TCAACATCAGT
miR-146a capturing DNA for MG-NP	HS-$(CH_2)_6$-A_{15}-PEG_6-AACCCATGGAA
miR-191 capturing DNA for MB-NP	HS-$(CH_2)_6$-A_{15}-PEG_6-CAGCTGCTTTTG
miR-141 capturing DNA for MB-NP	HS-$(CH_2)_6$-A_{15}-PEG_6-CCATCTTTACC
miR-155 capturing DNA for MB-NP	HS-$(CH_2)_6$-A_{15}-PEG_6-ACCCCTATCACG
miR-205 capturing DNA for IR-NP	GGAATGAAGGA-PEG_6-A_{15}-$(CH_2)_3$-SH
miR-125b capturing DNA for IR-NP	GGTCTCAGGGA-PEG_6-A_{15}-$(CH_2)_3$-SH
miR-191 capturing DNA for IR-NP	GGATTCCGTTG-PEG_6-A_{15}-$(CH_2)_3$-SH
miR-25 capturing DNA for IG-NP	CAAGTGCAATG-PEG_6-A_{15}-$(CH_2)_3$-SH
miR-21 capturing DNA for IG-NP	CTGATAAGCTA-PEG_6-A_{15}-$(CH_2)_3$-SH
miR-141 capturing DNA for IG-NP	AGACAGTGTTA-PEG_6-A_{15}-$(CH_2)_3$-SH
miR-221 capturing DNA for IB-NP	GACAATGTAGCT-PEG_6-A_{15}-$(CH_2)_3$-SH
miR-146a capturing DNA for IB-NP	TTCAGTTCTCA-PEG_6-A_{15}-$(CH_2)_3$-SH
miR-155 capturing DNA for IB-NP	ATTAGCATTAA-PEG_6-A_{15}-$(CH_2)_3$-SH

요약(국문초록)

바이오센싱 플랫폼으로서의 인지질이중층

나노입자의 반응을 단일입자 수준으로 관찰하는 것은 다양하고 복잡한 물리, 화학, 생물의 과정에 대한 직관적인 정보를 줄 수 있다. 하지만, 기존의 방법과 도구로는 의미 있는 관찰이 어렵다. 지지형 인지질이중막을 이용하면 이러한 문제점들을 해결할 수 있다. SLB는 세포막이 가지고 있는 중요한 생물학적 특징인 유동성, 세포막 성분과의 친화성 등을 그대로 유지한 인공 세포막으로 원하는 형태로 조립이 용이하다. 본 학위논문에서는 이차원 형태의 인지질이중막을 플랫폼으로 사용하여 광학적으로 안정한 플라즈모닉 금속나노입자의 행동을 관찰하고 유의미한 결과를 얻어내는 방법을 제시하도록 하겠다. 사용된 이차원 인지질이중막은 유동성을 가지며, 수많은 금속나노입자가 표면에 결합될 수 있다. 표면에 결합된 금속나노입자들은 각각의 움직임이 실시간으로 관찰 된다. 표면개질된 금속나노입자는 외부자극에 의해 특별한 행동이 유발 될 수 있다. 한 가지 예는 금속나노입자 표면을 DNA로 개질시키면 상보적인 서열은 갖는 DNA 혹은 RNA에 의해 결합될 수 있다. 플라즈모닉 금속나노입자들은 일정 거리 이하에 위치하는 경우 산란세기가 증폭되는 성질을 갖는다. 따라서 외부자극에 의해 금속나노입자들이 결합하는 현상을 실시간으로 관찰하며 추적할 수 있다. 본 학위논문에서는 이차원 지지형 지질이중막과 플라즈모닉 금속나노입자를 이용하여 바이오물질 검출 방법을 제시하도록 하겠다. 이외에도 다양한 표면개질을 통해 나노입자의 행동을 조절할 수 있음을 보여, 지지형 지질이중층이 바이오센서의 플랫폼으로 적합함을 확인할 것이다.

바이러스는 살아 있는 생명체를 감염시키고 해로운 질병을 유발할 수 있는

작은 매개체이다. 신속하고 민감한 바이러스 탐지는 공중 보건에 유익 할 것이며, 최근 연구들은 나노 입자가 바이러스 탐지에 응용될 수 있다는 것을 보여주고 있다. 특히, 국부적인 표면 플라즈몬(localized surface plasmons)에 기인하는 금속 나노 입자의 독특한 성질은 다양한 방법을 통해 바이러스의 검출을 가능하게 한다. 또한, 표면 개질의 용이성은 바이오 응용 분야에 이점을 제공한다. 제 1장에서는 항체를 부착한 나노입자를 지지형 지질 이중막의 표면에 연결하여 바이러스를 검지하였다. 바이러스의 농도에 따라 나노입자간 근접장 상호작용의 정도가 다름을 dark-field microscopy로 확인하였다. 이를 통해 미지 시료의 바이러스를 검지할 수 있음을 실험적으로 밝혔다.

반도체 기반 컴퓨팅 장치의 개발은 현대 사회를 변화 시켰다. 분자 컴퓨팅은 보완적 기술로 제안되었지만, 그 영향은 아직 미미하다. 기존의 방법은 실용성과 일반적인 적용성이 뛰어난 DNA에 크게 의존한다. 논리 게이트에서 신경망에 이르기까지 다양한 핵산 기반 계산이 증명되어왔다. 그러나 proof-of-concept을 넘어선 DNA 기반 장치의 실용적인 응용은 많은 한계점에 의해 진행되지 못하고 있다. 제 2장에서는 나노입자에 도입된 작용기의 화학적 특성과 지지형 지질 이중막의 유동성을 결합하여 새로운 형태의 정보처리 플랫폼의 가능성을 보였다. 금속 이온과 외부 환경에 의해 지지형 지질 이중막 상의 나노입자가 조립 및 분해됨을 확인하였다.

복수의 리간드와 수용체 사이의 결합 패턴과 화학적, 생물학적 시스템에서 보이는 특이적인 결합형성과 상호작용, 그리고 동일 환경에서 결합쌍의 종류에 따라 각기 다른 친화력과 속도론적 특징을 갖는 것에 대한 정보를 얻기 위해서는 다수의 분자와 입자들의 상호작용에 대한 실시간 다중분석이 필요하다. 특히, 정량적이고 신뢰성있는 수준으로 miRNA를 다중 프로파일링 하는 것은 세포생물학, 바이오센싱, 임상 진단 분야에서 miRNA를 사용하기 위해 크게 요구되고

있으며, 다수의 miRNA 서열이 특이적으로 분석되지 않는다면 이를 이용한 암 진단은 불가능하다. 제 3장에서는 높은 광안정성과 뚜렷한 광학 신호를 보이며, SLB위에서 역동적인 움직임을 갖는 광동역학적 나노프로브(optokinetically coded nanoprobes)를 이용하여 다중 분자 검지 방법을 제시하도록 하겠다. 다크필드 현미경 상에서 빨강, 초록, 파랑의 색을 나타내는 3종류의 금속 나노입자 각각에 3종류의 target miRNA half-complements를 도입하고 유동성을 갖는 2차원 SLB에 움직이는 형태(M-NP)와 고정된 형태(I-NP)로 붙였다. 3종류의 M-NP와 I-NP를 결합을 광동역학적으로 조합하면 다크필드 현미경을 통해 개별 입자 수준으로 관찰과 분석이 가능하며, 이를 통해 하나의 샘플에서 9종류의 miRNA를 구분하고 정량할 수 있다. 광동역학적 나노프로브를 기반으로 한 검지는 다수의 타겟 miRNA를 동시에 정확하고 특이적으로 검출하며, 한 시간 내로 결과를 준다. 이러한 특징은 다양한 종류의 암 진단에 사용될 수 있을 것이다. OK-NLB 검지가 single-base mismatch 실험에서 특이성을 보여주고, 헬라세포에서 추출된 RNA 샘플을 qRT-PCR으로 분석한 결과와 거의 일치함을 확인하였다.

주요어 : 지지형 지질 이중층, 나노입자, 바이오센서, 바이러스 검지,
리간드 컴퓨팅, miRNA 검지
학번 : 2014-22419